A growing soft robot with climbing plant–inspired adaptive behaviors for navigation in unstructured environments

Emanuela del Dottore, Alessio Mondini, Nick Rowe, Barbara Mazzolai

To cite this version:

Emanuela del Dottore, Alessio Mondini, Nick Rowe, Barbara Mazzolai. A growing soft robot with climbing plant–inspired adaptive behaviors for navigation in unstructured environments. Science Robotics, 2024, 9 (86), 10.1126/scirobotics.adi5908 . hal-04409233

HAL Id: hal-04409233
https://hal.inrae.fr/hal-04409233v1

Submitted on 5 Nov 2024

Del Dottore, E., Mondini, A., Rowe, N. and Mazzolai, B., 2024. A growing soft robot with climbing plant–inspired adaptive behaviors for navigation in unstructured environments. *Science Robotics*, *9*(86), p.eadi5908.

Title: A growing soft robot with climbing plant inspired adaptive behaviors for navigation in unstructured environments

Authors:

Emanuela Del Dottore,[1]*† Alessio Mondini,[1]† Nick Rowe,[2] Barbara Mazzolai[1]*

Affiliations:

[1]Bioinspired Soft Robotics Lab, Fondazione Istituto Italiano di Tecnologia, Genova, Italy

[2] AMAP, Univ Montpellier, CIRAD, CNRS, INRAE, IRD, Montpellier, France

***Corresponding author(s): emanuela.deldottore@iit.it; barbara.mazzolai@iit.it**

† These authors contributed equally to this work

Abstract:

Self-growing robots are an emerging solution in soft robotics for navigating, exploring, and colonizing unstructured environments. Yet, their ability to grow and move in heterogeneous three-dimensional (3D) spaces, comparable to real-world conditions, is still challenging. We present an autonomous growing robot that draws inspiration from the behavioral adaptive strategies of climbing plants to navigate unstructured environments. It mimics their apical shoot to sense and coordinate additive adaptive growth via an embedded additive manufacturing mechanism and a sensorized tip. Growth orientation, comparable to tropisms in real plants, is dictated by external stimuli, including gravity, light, and shade. These are incorporated within a vector field method to implement the preferred adaptive behavior for a given environment and task, such as growth towards light and/or against gravity. We demonstrate the robot's ability to navigate through growth in relation to voids, potential supports, and thoroughfares in otherwise complex habitats. Adaptive twining around vertical supports can provide an escape from mechanical stress due to self-support, reduce energy expenditure for construction costs, and develop an anchorage point to support further growth and crossing gaps. The robot adapts its material printing parameters to develop a light body and fast growth to twine on supports or a tougher body to enable self-support and cross gaps. These features, typical of climbing plants, highlight a potential for adaptive robots and their on-demand manufacturing. They are especially promising for applications in exploring, monitoring and interacting with unstructured environments or in the autonomous construction of complex infrastructures.

One-Sentence Summary:

A growing plant-like robot with adaptive behaviors able to grow, morph and navigate in unstructured environments.

Main Text:

INTRODUCTION

Autonomous robot navigation outside laboratory conditions entails carrying energy-expensive sensors and controllers. This has made it problematic to limit the size of robots and keep necessary computations simple. Growing robots are a class of soft robots (*1*, *2*) that adaptively implement apical addition of material to build their bodies (*3*). They show some basic developmental similarities and advantages as plant stems and roots, plant pollen tubes, and fungal hyphae. Such plant-like functioning is especially capable of safely navigating diverse unstructured domains. This is a key attribute, making them a valuable alternative to flying, wheeled, or legged robots. Apical growth enables robot navigation in both above- and below-ground environments (*4*, *5*) and penetration of dense media such as soil (*6*, *7*). Apical growth also means that stem-like bodies can avoid and negotiate unpredicted obstacles (*8–10*) and maneuver in different types of terrain (*11*). In addition, growing robots solve the energy supply problem by being inherently tethered (*12*).

Approaches to enable artificial growth include pneumatically-driven skin eversion (*5*, *8*, *13–15*); pressurized elongating tubes (*16*); chain locking blocks mechanism (*17*); and additive manufacturing (*6*, *9*, *10*, *18*).

Additive manufacturing, in particular, has brought about a substantial transformation in the conceptualization and prototyping of complex three-dimensional (3D) models and has had a profound influence on robotics (*2*). Robotics has leveraged this technology to construct infrastructures, for example, with the use of a swarm of robots (*19*), as well as fabricate robot parts with functional soft materials (*20*) that result in more dependable structures with fewer assembled components and enhanced biomimetic behaviors (*21*).

Despite these recent innovations, the embodiment of additive manufacturing for effective motion in unstructured 3D environments remains challenging in growing robots. This is particularly true if autonomous and adaptive dynamic responses are needed to respond safely to changing environmental conditions. Regarding the physical environment, the robot must switch movement modalities to overcome voids, climb supports, navigate across different terrains on or near the ground, and navigate through different kinds of clutter.

Mechanical self-loading of growing robots, resulting in suspended bodies and end-loading of an exploratory tip, can lead to failure and collapse due to structural weakness. For this reason, robots with elongated bodies and an exploring apical head risk being restricted to moving along the ground and limited or unable to span voids (*11*, *13*). Alternative implementations acting on the ground risk having limited maneuverability. For instance, obstacles and narrow spaces can physically interfere with and block protruding robot mechanisms and lateral appendages, locking the forward motion of a growing apex or head (*18*). Moreover, existing growing robots have limited autonomous decision-making capabilities to deal with unforeseen environmental conditions.

In contrast, there are living organisms that can move and act in challenging surroundings with slender, self-loading bodies and a decision-making apex in which additive, adaptive growth ensures safe and forward movements. Climbing plants are natural explorers and have evolved numerous and different habits to exploit diverse ecological habitats (*22–24*). They are already a source of inspiration in robotics (*5*, *11*, *12*, *25–28*), generating a class of robots named GrowBots (*29*, *30*) or Vine robots (*27*). These robots are generally based on imitating a few selected features of plant climbers, such as oscillatory searching movements (*27*), anchoring by hooks and prickles (*26*), or tendril appendages (*29*, *31*). Climbing plant-like robots have also incorporated intertwining of separate individual stems for posture control and stability (*29*) or use thin bodies with tip extensions for growth (*5*).

Instead of isolating an individual feature, adopting an integrated view of climbing plants by considering their diverse ecologies and evolved functional traits would facilitate more precise matching or "phenotyping" a technical device with its environment. Such an approach will also provide more varied design specifications for more diverse, adaptive robots.

Plants have neither vision nor a central brain, yet they display directional growth and functional adaptations to environmental cues in changeable and challenging environments. The shoot apex is the region where active cell division within the meristem and subsequent cell elongation occurs, leading to the overall growth and extension of the plant body as induced by multi-sensory perception-action loops located in the apex (Figure 1A). During the apical processing of external signals, cells near the apex develop unevenly and differentially elongate, resulting in environmentally mediated directional growth (tropismss) (*36*). Photoreceptors and gravity-sensing cells are distributed throughout the apical shoot and are involved in phototropic (*32*, *33*) and gravitropic responses (*34*, *35*), respectively. In order to locate, reach and interact with obstacles and potential supports, climbing plants produce an initial self-supporting stem whose stiffness and density decrease adaptively following location and attachment to an external support (*37*, *38*). It has been suggested that support localization by plants is driven by attraction to shade (*39–41*). This is known as skototropism or negative phototropism. It is guided by a low red to far-red ratio, which is related to dense vegetation (*42*). After attaching to a host tree, climbing plants grow against gravity using the tree as a support. Once the top is reached, positive phototropism (growth towards blue wavelength from light) can be restored. Correctly orchestrating such shifts in behavior is crucial to plant survival (*37*).

Robotic translation of this close relationship between plant-like sensing and actuation would benefit morphological adaptation in growing stem-like robots. It would, for example, enable adaptive extension across 3D spaces, twining around supports, crossing voids, and fine-tuning the geometry and mechanical properties of the artificial stem for specific environmental conditions. However, robot embodiment of adaptive movements through additive growth processes guided by online multi-sensory perception-action loops remains underexplored today.

This article presents a climbing plant-inspired robot named FiloBot. The robot builds its own stem-like body using a polylactic acid (PLA) thermoplastic material with an embodied Fuse Deposition Modeling (FDM) technique. The robot reacts to environmental constraints and stimuli through a combination of passive morphological adaptation and a bioinspired behavior-based control that uses a vector field method to estimate multi-tropism-induced growth directions in the apical head. This empowers the robot's capabilities for exploring different 3D spaces (Movie 1). Figure 1A-B shows the analogy between the biological model and the robot regarding apical, meristematic growth, and sensing-actuation. As in plants (Figure 1C-E), the robot perceives gravity and the intensity and direction of blue, red, and far-red light and implements various perception-action loops (Figure 1F-H), navigating the environment by adapting its morphology without pre-programmed movements, path planning, or teleoperation. Light can induce positive phototropisms and skototropisms. The robot uses skototropisms to locate and grow toward supporting structures (plant Figure 1C against robot Figure 1F). Gravity plays a crucial role as a reference for the robot's orientation, enabling gravitropic behavior (plant Figure 1D against robot Figure 1G) and climbing vertical supports by twining (plant Figure 1E against robot Figure 1H). As in plants, FiloBot can adaptively fine-tune the mechanical properties of its stem-like body in relation to the environment and the required task. These include three main functional criteria. A strong and tough body to self-sustain its body when in suspension, a lighter body with less energy costs when attached to a support, and faster growth when twining and

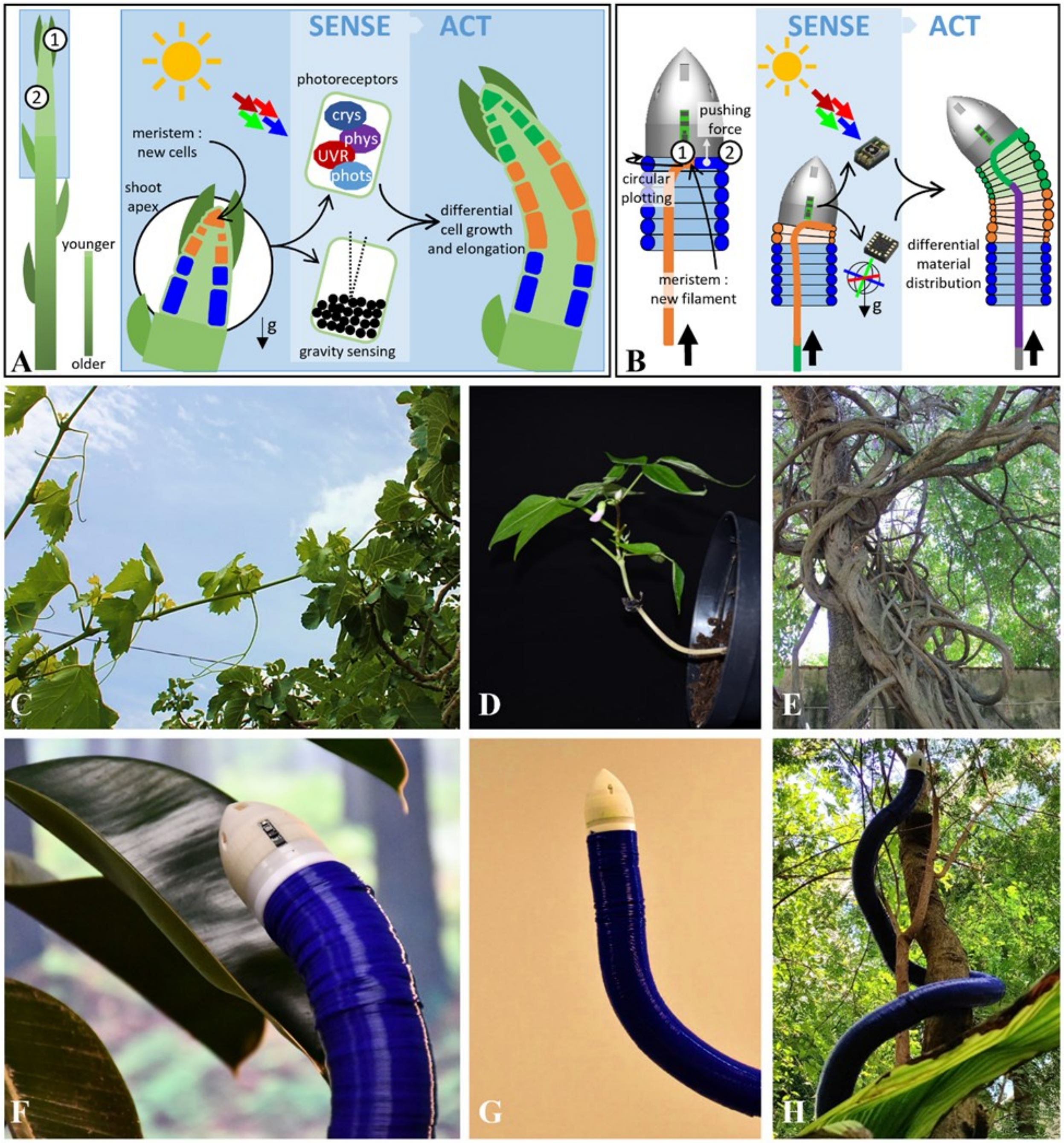

Fig. 1. Examples of adaptive growth in climbing plants and the robot. Sketch of the bioinspired sensing and actuation mechanisms. **(A)** Simplified representation of the growth zones, their functions, and growth responses. The shoot apex comprises layers of cells that constitute the meristematic part (point 1) and the cell elongation region (point 2). Photoreceptors and gravity-sensing cells are distributed within the shoot apex. Perception of external signals is thus localized in the apical part, where actuation is also implemented. Processing of an external stimulus dictates cell growth, elongation, and the resulting orientation of the shoot. In the example, photo-perception defines the shoot movement towards light merged with gravity perception against gravity. **(B)** Schematic representation of the growing robot regions, their functionalities, and growth responses. Analogous to the shoot apex, the robot comprises sensing elements and a material deposition region localized at its head (points 1 and 2). In the meristem-like region, there is the plotting of new

material and the generation of forces needed to propel the tip forward. Control of the plotting defines either a lower or higher material layer along the stem axis analogous with differential cell division and elongation. In analogy with the biological model, the robot processes sensory inputs and defines a differential material deposition both towards light and against gravity. In both the natural and artificial models, the already grown part of the body no longer moves or re-orientates with respect to the environment. **(C-E)** Examples of plant body shapes and behaviors in climbing plants. **(F-H)** FiloBot mimics the same behaviors. **(C)** and **(F)** represent skototropisms, involving growth directed towards shaded areas beneath leaves. In **(C)**, the stem of a vine plant spans over a void to reach a fig tree. Likewise, our robot can recognize the presence of shade beneath a plant and grow towards it **(F)**. **(D, G)** represent gravitropism, meaning directed growth against gravity, in a lab-grown bean plant **(D)** and with the robot **(G)**. **(E)** Complex growth behaviors of plants on supports. **(H)** A laboratory-grown FiloBot stem juxtaposed with real plants in a woodland habitat indicating the similarity of size, shape, and scale of natural plants and the robot.

moving along a support. By varying the material deposition parameters of the additive manufacturing mechanism, the stiffness of the body structure can be fine-tuned along with an adaptive control of energy expenditure.

These features and capabilities enable the growing robot to navigate unstructured 3D environments adaptively with an efficient yet simple control. This minimizes construction costs in terms of energy and material and maximizes simplicity for sensing and computing strategies. This enabled our climbing plant-inspired robot to carry out autonomous 3D navigation in real-world scenarios.

RESULTS

We have developed a self-growing robot that mimics the adaptative and environment exploration strategies of climbing plants. We show the robot can manage different scenarios and be resilient to unexpected hindrances and general perturbation. The robot can negotiate voids, anchor itself to vertical supports by twining, and navigate the environment through a behavior-based control inspired by tropism behaviors of plants (Movie 1). Diverse body shapes and mechanical properties are also generated as adaptive robotic “phenotypic expressions” while negotiating a heterogeneous environment during growth.

To achieve these results, we underwent a redesign of our previously developed growing robot (*6*), reducing dimensions and improving its minimum bending radius. A control strategy for material deposition was also implemented to accommodate the design and allow steering of the system.

Growing robot with configurable bodies: working principle and characterization

Building on our previous works (*6*, *9*), we embodied a material extrusion process, Fused Deposition Modelling (FDM), into a robotic system (FiloBot) to create artificial apical growth. FiloBot comprises an apical robotic head for thermoplastic material deposition and sensing, a stem-like body produced by the growth from the apical head region, and a basal station with a power supplier, filament spooler, and fans (Figure 2A). The robot is detailed in Materials and Methods. It achieves an autonomous online configuration of its body through the embodiment of additive manufacturing. The resulting body is unique to each deployment, defined by robot-environment interactions. The thermoplastic filament is pulled from the base into the heating channel at the head and is extruded in a circular profile

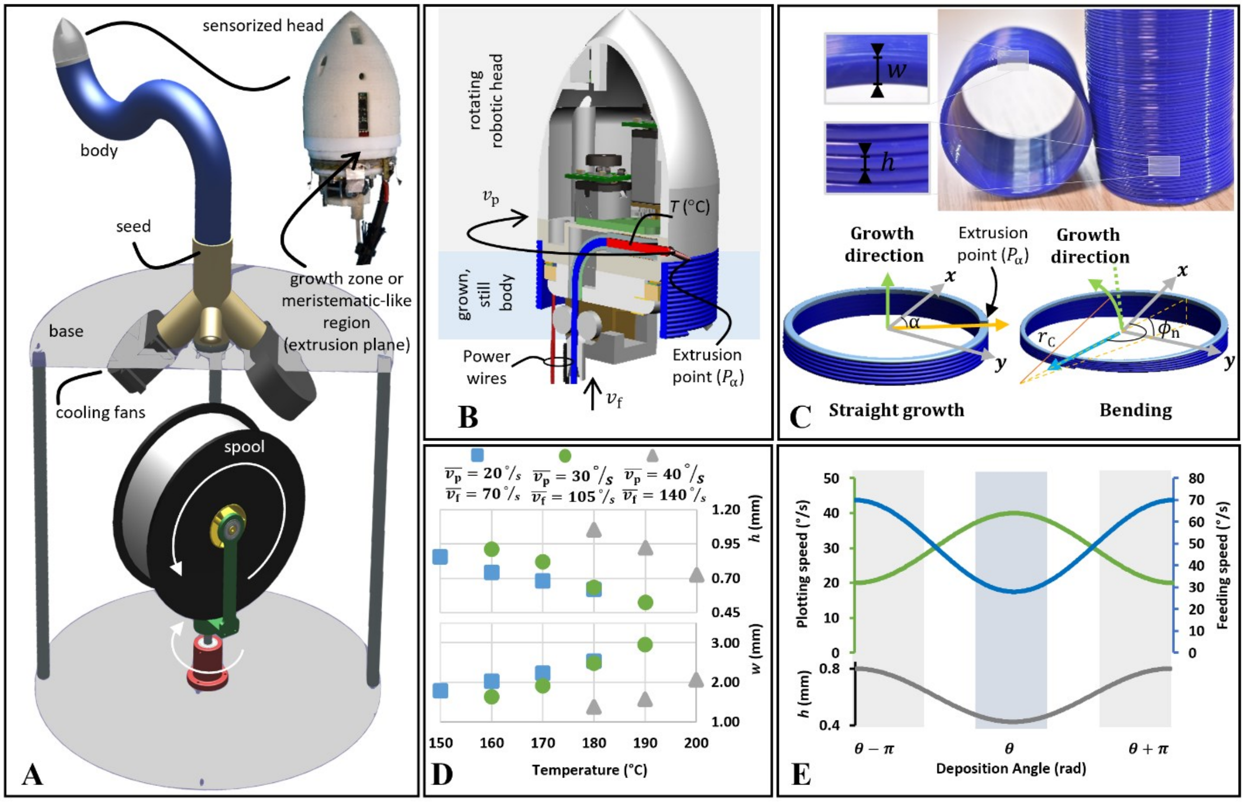

Fig. 2. FiloBot overall system and characterization. (A) CAD of the overall FiloBot system, including the robotic head, the grown body structure, and a basal station. The base contains the seed (an initial precursor for the structure) connected to two cooling fans and a spooler that passively releases the 3D printing filament from a commercial spool (white arrows indicate its degrees of freedom). The prototyped robotic head is shown. It assembles a Fused Deposition Modeling-based 3D printing plotting mechanism with a sensorized control board. **(B)** The basic working principle, with three control parameters: speed of the incoming filament (v_f), speed of the rotating plotting (v_p), and heating temperature (T). **(C)** A picture of a straight-grown body with the height (h) and width (w) of the deposited layer. The drawings show a straight growth with the robot's coordinate frame (gray arrows), the growth direction (green arrow), and the extrusion point vector (yellow arrow) that moves circularly. Layers are deposited with a uniform height and width; and a bending with the robot's coordinate frame (gray arrows), the growth direction (green arrow), the vector corresponding to the bending direction θ (light blue arrow), the magnitude of the bending over n deposited layers ϕ_n, and the curvature radius performed r_c (orange line). **(D)** Height and width in straight growth with different printing parameters. **(E)** The control law imposed on the feeding and plotting motors produces a differential material deposition with a minimum layer height at θ and a maximum layer height at $\theta + \pi$.

(Figure 2B). The material extrusion creates a lift force sufficient to propel the robotic tip forward, thus implementing a plant-like apical growth through material addition from the tip. The malleability of the thermoplastic material during deposition allows for the extrusion of the filament in layers that vary with three control parameters: extrusion temperature (T), plotting (v_p), and feeding (v_f) speed (Figure 2B). Different combinations of these parameters create different homogeneous stem-like bodies as tubular structures with various geometrical (Figure 2C and Figure S1) and mechanical characteristics. The robot performs straight growth with no external forces and constant feeding and plotting speeds. The filament is deposited in layers with a constant height (h) and width (w), with h decreasing and w increasing with increasing temperature (Figure 2D and Table S1). In straight growth, we tested combinations of control parameters allowing axial growths approximately from 2 mm/min to 7 mm/min (Table S1). Inherent characteristics of additive manufacturing processes dictate the achievable axial growth speeds (see Supplementary Materials for considerations on the growth speed). The system can steer by tuning the amount of material deposited around the circumference. FiloBot achieves this via a velocity control on both feeding and plotting motors (Figure 2E and Table S2). The control law targets a desired layer height for each point (P_α with $\alpha = 0, \dots, 2\pi$) around the circumference:

$$h(\alpha) = h_2\left(1 - \frac{I}{2}(1 + \cos(\alpha - \theta))\right), \tag{1}$$

where θ is the direction of bending, h_2 is the maximum height of the layer located at $\theta + \pi$, h_1 is the minimum height of the layer located at θ, and I is the bending intensity. If $I = 0$, a straight growth is obtained. Bending is achieved with an intensity where $I > 0$.

During robot motion in real-time, I is calculated proportionally to the stimulus-response intensity decoded in the desired bending angle ϕ defined through the bioinspired control. This angle is then transformed into the relative intensities I_f and I_p (Figure S2) to command the feeding and plotting motors, respectively, whose control laws comply with eq. (1):

$$v_\mathrm{f}(\alpha) = \bar{v}_\mathrm{f}\left(1 - \frac{I_\mathrm{f}}{2}(1 + \cos(\alpha - \theta))\right), \tag{2}$$

$$v_\mathrm{p}(\alpha) = \bar{v}_\mathrm{p}\left(1 + \frac{I_\mathrm{p}}{2}(1 + \cos(\alpha - \theta))\right). \tag{3}$$

In eq. (2) and (3), $\bar{v}_\mathrm{f}$ is the maximal feeding speed, and $\bar{v}_\mathrm{p}$ is the minimum plotting speed. These are the nominal speeds used to grow straight (Table S1). $v_\mathrm{p}(\alpha)$ reaches its maximum:

$$v_\mathrm{p}(\theta) = \bar{v}_\mathrm{p}(1 + I_\mathrm{p}), \tag{4}$$

and $v_\mathrm{f}(\alpha)$ reaches its minimum:

$$v_\mathrm{f}(\theta) = \bar{v}_\mathrm{f}(1 - I_\mathrm{f}), \tag{5}$$

in the bending direction (θ) to decrease the amount of material extruded (h in Figure 2E). Having three controllable parameters and two degrees of freedom (θ and ϕ), the robot can be treated as a mobile holonomic system (*43*) whose workspace is defined by its minimum curvature radius r_c (see Supplementary Materials for a workspace evaluation). The FiloBot's geometrical r_c is 47.83 mm (Figure S3A). However, its real achievement is constrained by the ability of the system to deposit the material on opposing flanks of its stem-like body differentially. In our tests, we reached a maximal $h_2 - h_1 = 0.29$ mm, leading to the minimal $r_\mathrm{c} \cong 80$ mm (Table S2 and Figure S3B).

High stress-resistant bodies enable void crossing

Climbing plants adapt their growth by producing rigid stems when they need to span between supports or increasing flexibility if the stem is under excessive mechanical stress (*22*). In our robot, different structural features are obtained by tuning the three control parameters described above (Figure 3A). A specific combination of parameters can be selected according to any specific scenario the robot encounters. The feeding speed can be increased without increasing the extrusion temperature to extrude a cold filament. This filament does not change viscosity at its core and is less compressible but has a weak bond with the previous layer. This strategy accelerates the growth speed of the robot (Table S2).

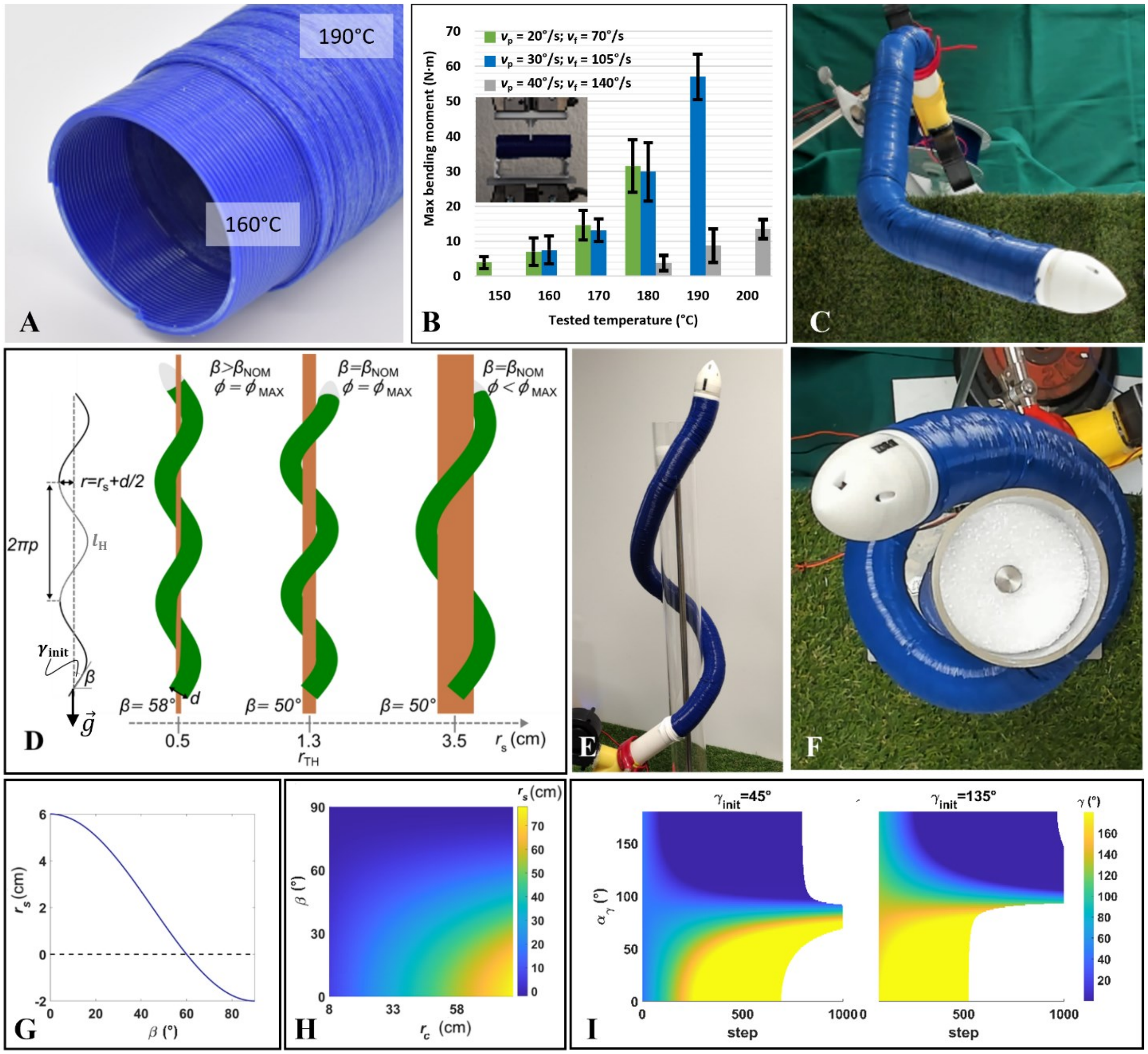

Fig. 3. Climbing plant-inspired behaviors in FiloBot. (A) A sample of a built structure where there is a passage between different printing parameters: from v_p=30°/s, v_f=105°/s, at 160°C to v_p=30°/s, v_f=105°/s, at 190°C. The higher temperature has produced thinner layers with a larger width, showing stronger bonding. **(B)** Maximal bending moments achieved via 3-point bending tests (inset) on stem-like structures generated using different plotting parameters. **(C)** Growth across a void. The final displacement in this experiment was 50 cm. **(D)** Three helical growth patterns simulated with different support radii and initial tip inclinations. The helical growth parameters are shown on the left. **(E)** Growth via twining with a support of 7 cm diameter and a helix slope angle of $\beta = 50°$. **(F)** Aerial view of the robot in a twining configuration. **(G)** Maximal support radius as a function of β considering $r_c = 8$ cm. **(H)** Evaluation of maximal support radius varying helix inclination and curvature radius. **(I)** Variation of tip inclination (γ), given as examples two different initial inclinations (γ_{init}), when an offset (α_γ) is applied to the growth direction $\theta = \alpha_g + \alpha_\gamma$. α_g defines the direction to follow gravity.

In contrast, slowing the feeding speed but maintaining a constant extrusion temperature over-melts the filament, which is then extruded with a smaller vertical thickness. This effectively slows the growth speed and allows the construction of more robust stem-like structures (Figure 3B and Table S3), which can also form a sealed pipe organization but with variable adapted shapes.

The highest body strength (57 N·m ± 6.51) was obtained in experimental tests using a plotting speed of 30°/s, a corresponding feeding speed of 105°/s, and a temperature of 190°C (Figure 3B). These settings ensure long extensions over voids without the risk of the robot's body collapsing. The body can self-sustain and carry additional loads if needed (Figure 3C and Table S3).

In general, the Young's modulus of liana stems has been estimated to vary ~2-13 fold from young to mature stages of growth, with higher stiffness at a young age when self-support is necessary for exploring and reaching supports (*44*). Similarly, in the robot, we found a 9-fold variation from the lowest (setting 150°C, $v_{\mathrm{p}} = 20$°/s, $v_{\mathrm{f}} = 70$ °/s) to the highest (setting 190°C, $v_{\mathrm{p}} = 30$°/s, $v_{\mathrm{f}} =105$ °/s) values of calculated Young's modulus among all the tested settings (Table S3). Generally, an initial stiffer, self-supporting, young stage of our robot is achieved via settings at higher temperatures, whereas less stiff properties typical of more mature flexible stems are constructed via lower temperatures. Implementing less rigid bodies results in an energetically efficient strategy (Table S4), allowing the robot to exploit proximal structures to anchor itself.

Twining climber robot with a gravity-based feedback control

A typical habit of twining plants involves a helical growth of the stem, which is adapted to wrap around supporting structures and—at the same time—grow vertically to reach higher exposure to light. This growth habit is a mechanism that can prevent the plant from falling because of the resistance to forces perpendicular to the support. Helical paths are characterized by the pitch (*2πp*) of the helix and the radius (r) (Figure 3D). In our case, *r* is the sum between the support radius (r_{S}) and the growing structure radius ($d/2$). These parameters define the spiral length (l_{H}), the slope angle (β), the curvature (k), and the torsion (τ) (*45*, *46*):

$$l_H = 2\pi\sqrt{r^2 + p^2};\quad \tan\beta = \frac{p}{r};\quad k = \frac{r}{r^2+p^2};\quad \tau = \frac{p}{r^2+p^2}. \tag{6}$$

The additive manufacturing process adopted by our growing robot entails depositing material in a series of layers. Dividing the spiral length by the average layer height (h) gives the number of layers needed for a whole spiral ($N = l_{\mathrm{H}}/h$). By keeping the bending direction (θ) constant, a curve in a plane is obtained. To obtain a spiral, θ should vary linearly at each slice over a spiral period:

$$\theta_{i+1} = \theta_i + \frac{\beta}{N} \tag{7}$$

In this case, the bending angle ϕ of each layer can be derived from the curvature of the helix:

$$\phi = kh. \tag{8}$$

The maximal curvature constraint ($k_{\mathrm{MAX}} = 1/r_{\mathrm{c}}$) leads to the following conditions:

$$k = \frac{1}{\left(r_{\mathrm{S}}+\frac{d}{2}\right)(1+(\tan\beta)^2)} < k_{\mathrm{MAX}},\ \tan\beta > \sqrt{\frac{1}{\left(r_{\mathrm{S}}+\frac{d}{2}\right)k_{\mathrm{MAX}}} - 1}. \tag{9}$$

Considering these conditions, different climbing strategies can be implemented as a function of the support radius (Figure 3D). When a nominal climbing slope angle (β_{NOM}) used as default by the robot to wrap around support ($\beta = \beta_{\mathrm{NOM}}$) is fixed, k and consequently ϕ vary with the dimension of the support ($\beta = 50°$ in the example shown in Figure 3E-F). This climbing strategy can be adopted until a threshold radius (r_{TH}) is achieved, which is associated with the maximum reachable curvature (k_{MAX}). In our case $r_{\mathrm{c}} = 80$ mm and

$d/2 = 20$ mm, consequently β needs to be less than 60° (Figure 3G) to wind around supports with:

$$r_\mathrm{S} = \frac{r_\mathrm{c}}{1+(\tan\beta)^2} - \frac{d}{2} > 0, \tag{10}$$

otherwise, a tortuous path is formed (Video S1). For low r_S, β needs to be high to enable wrapping around the support (Figure 3H). On the other hand, supports with a large radius need a large curvature radius (Figure 3H) that reduces the anchoring efficiency as long paths are generated. These observations are in agreement with biological investigations that have found adaptive twining behavior for supports of different diameters (*37*), where the ascending angle (β) decreases with increasing support diameter eventually becoming unstable for large supports ($r_\mathrm{c} < r_\mathrm{s}$).

Theoretically, by knowing the support radius, we can control the direction of the growing robot by varying the bending direction following eq. (7) with a constant bending intensity (eq. (8)). However, in real conditions, the support radius cannot be known in advance.

Gravity is a key feedback signal for plants. When deprived of endodermal gravisensing cells, twining plants cannot grow upward nor twine around supports (*47*). Inspired by this behavior, we exploited gravity to create an absolute reference for the robot and set the bending direction from it:

$$\theta = \alpha_\mathrm{g} + \alpha_\gamma. \tag{11}$$

α_g is the angle corresponding to the projection of the gravity vector into the *xy*-plane of the robot, and α_γ is an offset. Given an initial inclination with respect to gravity (γ_init in Figure 3I) and by providing different α_γ, it is possible to achieve various behaviors. Video S2 shows examples of the robot initially directed upward ($\gamma_\mathrm{init} = 45°$) and downward ($\gamma_\mathrm{init} = 135°$). Specifically, if $\alpha_\gamma = 0°$ or $\alpha_\gamma = 180°$, the robot aligns with the gravity vector. In the first case, it grows downward as in positive gravitropism in plants, visible in roots. In the second case, it grows upward, mimicking negative gravitropism visible in the aerial part of plants. For $\alpha_\gamma = 90°$, the robot grows helically, as in the twining behavior of climbing plants, with a constant radius around the central gravity axes. This offset is used in our robot to twine around a vertical support (Video S3), potentially saving it from falling due to disturbances perpendicular to the support or being pulled away from a support laterally by its own weight or by some other disturbance. For $\alpha_\gamma \neq 90°$, the robot performs spiral-like paths with a variable radius. If the robot is initially directed downward, and $0° < \alpha_\gamma < 90°$, the radius decreases over time and with a rapid tendency to straighten its path downward (attracted by gravity). If the robot is upward oriented, the spiral has an increasing radius until it inverts the trend and reaches the downward direction, showing positive gravitropism. For $90° < \alpha_\gamma < 180°$, the robot manifests a strong negative gravitropism. The spiral decreases its radius if the robot is initially upward-directed, fast approaching a straight path. In contrast, the spiral increases its radius if it is in a downward configuration until inverting its growth direction. This offset can thus approximate the specialization of differently behaving organs (positive or negative gravitropism, typical of roots and stems) and fine-tune them similar to the responses via physiological adaptive processes in plants.

Environmentally mediated behaviors for robot navigation

Adaptive behaviors in many plant species and individual plant organs often include tropisms. In aerial parts of plants, especially growing stems, the initial tropism of young growth is a negative tropism against gravity. Shortly afterward, a further response concerns environment exploration to increase exposure to light and facilitate photosynthesis via a

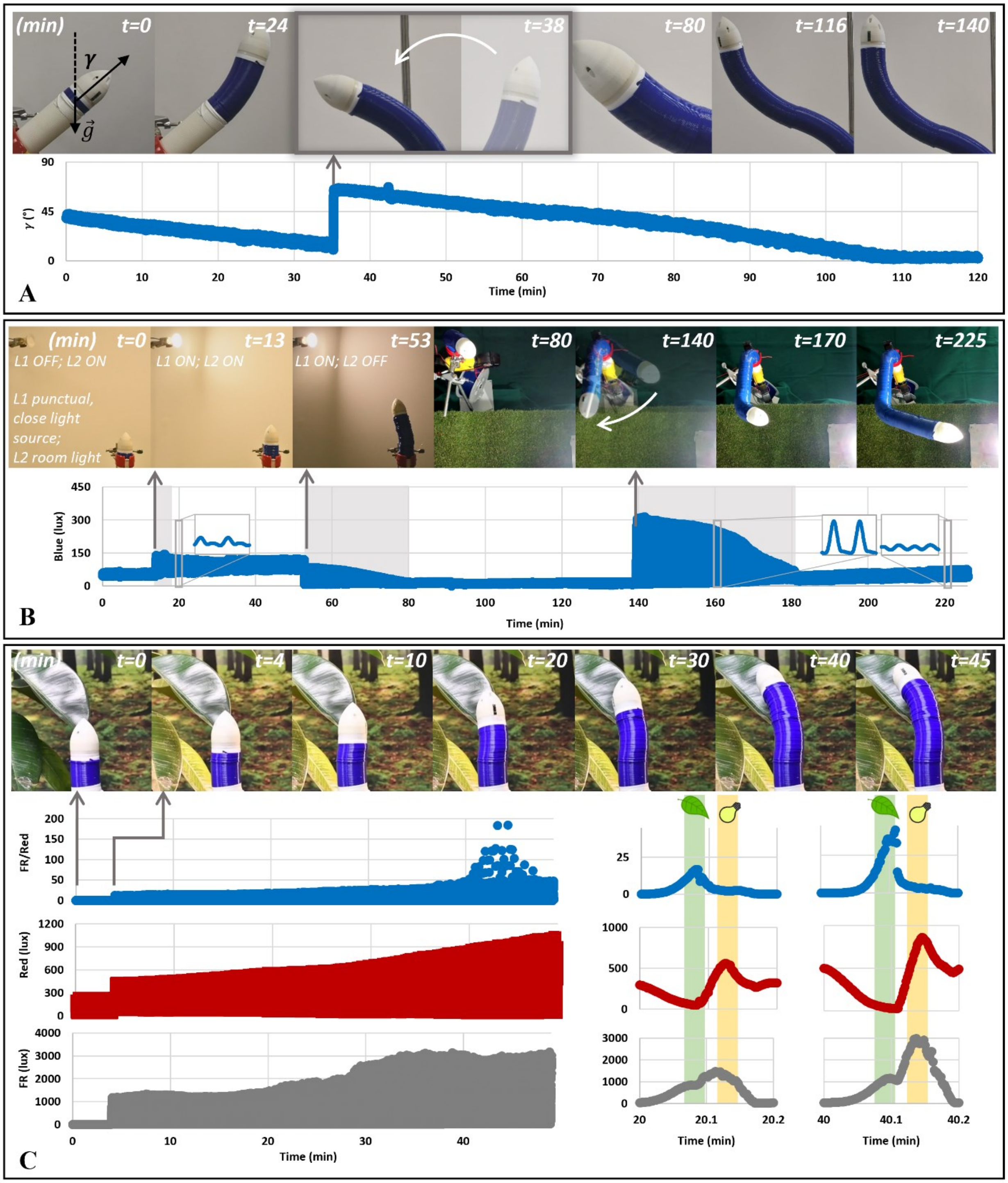

Fig. 4. Environmentally driven behaviors in FiloBot. (A) Result of a negative gravitropic response on the robot. The sequence of frames is associated with the corresponding tip inclination change over time. The robot immediately recovers gravitropism with upward growth after a perturbation consisting of its sudden repositioning at $t = 38$ min. **(B)** Result of a positive phototropic response on the robot. The sequence of frames of the FiloBot is associated with the robot's perception graph of blue light, showing different light settings in the environment and how perception varies with the tip orientation to light. The inset graphs show three 0.5 min close-ups where two full deposition cycles are accomplished (y-axis range is [0, 300] lx). In the first inset from the left, two peaks in one cycle are visible (due to two different light sources: L1 close light source and L2 room light). The second inset has only one peak (a

single light source, L1). The gray background indicates where the robot perceives a predominant direction of light intensity. In the other regions, the robot perceives a more or less similar value all around its circumference (third inset with small oscillations). **(C)** Result of skototropic response. The sequence of frames shows the directed growth towards plant leaves after the *FR* light emitter has been switched on (t = 4 min). The graphs show the ratio between *FR* and red light signals, the red and *FR* signals individually, and two zooms for each signal at 20 and 40 min. From 20 to 40 min, intensity values increase due to closer proximity to both the light emitter and leaves.

positive response to blue/UV light. These two tropisms can strongly interact, each enhancing or reducing the effects of the other (*48*). The gravity response can be described by the distribution of the curvature rate of the shoot, which depends on the initial stimulation angle (γ) with a sine law (*49*, *50*). In our case, the curvature rate is given by the ϕ of a differential growth, which we implemented for the gravitropic response (ϕ_{g}) equal to:

$$\phi_{\mathrm{g}} = \bar{\phi}\, sin|\gamma|, \tag{12}$$

where $\bar{\phi}$ is the maximum achievable bending rate relative to one deposition cycle, and γ is the inclination of the tip at each cycle with respect to gravity. For a faster response in robotic exploration and navigation, this response can be accelerated by setting $\phi_{\mathrm{g}} = \bar{\phi}$ until a low threshold for γ is reached (Figure 4A, Video S4). The direction θ_{g} is instead obtained as $\pi + \alpha_{\mathrm{g}}$.

In positive phototropism, there is a positive curvature – growth towards the light. The curvature response typically shows two characteristic positive peaks (*51*). The first is close to the coleoptile tip and complies with the reciprocity law (proportionality between irradiance and time of exposure, *I*×*t*). The second extends farther down the tip with a linearly time-dependent response (with no intensity influence). Since our robot cannot elongate the material already deposited, the robot can only implement the first positive phototropic response. In our robot, we set the rate of curvature in response to light as:

$$\phi_{\mathrm{p}} = \bar{\phi}\frac{|s_{\mathrm{p}}|}{\sum_{i=1}^{N} b_i}, \tag{13}$$

$$s_{\mathrm{p}} = \sum_{i=1}^{N} b_i \hat{\imath}, \tag{14}$$

where $|s_{\mathrm{p}}|$ is the norm of the resulting vector of the blue light intensity obtained as the sum of the vector field over one scanning cycle. In eq. (14), N is the number of acquisitions in one cycle, and b_i is the blue light intensity perceived along the direction $\hat{\imath}$. The intensity is normalized between 0 and 1 with respect to the accumulated blue light incoming in one cycle. The direction to growth to (θ_{p}) is defined by the arctan of the x and y components of s_{p}. The robot successfully responded to the light stimulus with an irradiance-response curve actuated at the apex during the first positive phototropism until perceiving a non-directional, reduced light intensity due to the apex reaching the close vicinity of the light source (Figure 4B, Video S5). It also combines multiple light sources and follows the preferential growth direction given by the field of attraction, displaying a less evident directionality towards the punctual light ($t < 53$ min in Video S5 and Figure 4B) compared to the marked light-oriented growth manifested in the presence of a single light source ($t > 53$ min).

Skototropism defines the attraction to shaded areas related to the presence and amount of vegetation (*42*). In climbing plants, skototropism is hypothesized to help the localization of possible hosts (*37*, *52*). The attraction towards the host is driven by a low red (R) to far-red (FR) signal ratio. In the robot, we used the FR : R to produce an attractive skototropic vector field around the robot's tip. The attractive vector s_{k} is obtained as in eq. (15), with an intensity ϕ_{k} (eq. (16)) normalized between zero and one with respect to the accumulated FR : R signal incoming in one cycle.

$$s_{\mathrm{k}} = \sum_{i=1}^{N} \frac{FR_i}{R_i} \hat{\imath}, \tag{15}$$

$$\phi_{\mathrm{k}} = \bar{\phi} \frac{|s_{\mathrm{k}}|}{\sum_{i=1}^{N} \frac{FR_i}{R_i}}. \tag{16}$$

The growth direction (θ_{k}) is defined by the arctan of the x and y components of s_{k}.

Readings from the robot show a minimum peak of the R signal in correspondence with the plant direction and a maximum peak in the presence of the lamp (Figure 4C), demonstrating the absorption of red by the leaves. At the same time, the FR signal has two maximal peaks, a lower one in correspondence with the plant and a higher one in correspondence with the lamp direction. This perception produces a greater attraction field towards the plant, expressed in the directed growth achieved with the robot, and results in reaching behavior (Figure 4C, Video S6).

In order to abstract different tropic behaviors, tropisms can be combined by summation, each with different weights (*52*). Additionally, tropisms, twining, and crossing gaps can all be switched to achieve rich task-oriented behaviors. A demonstration is shown in Video S3, where the robot transits from twining behavior to negative gravitropism at the end of the support. However, orchestrating these behaviors is not trivial in plants that can accomplish complex growths (Figure S4). These complex growth patterns might arise from combining simpler behaviors with dynamically adapting individual contributions (*53*). Although biological mechanisms still need deep investigations, we have extracted basic working principles akin to a behavior-based control applicable to our growing robot in this work. With simple stimulus-response rules, this behavior-based control can direct 3D navigation in virtually any unstructured environment where some attractive targets can be defined. It also emerges as an intrinsic resilience in the control strategy, allowing the robot to restore a task without dedicated control of fault occurrences but relying on its external perception and current state. Examples of this feature are shown in Figures 4A and B, where the FiloBot autonomously adjusts its growth direction, following gravitropism and phototropism after being repositioned in space.

DISCUSSION

Autonomous, adaptive robotic systems are highly desirable for operating in unpredictable, unstructured scenarios. The decision-making required to pilot robots in such situations is similar to how climbing plants find their way from the ground to the top of a forest via unpredictable obstacles, voids, and supports. Many potential applications can benefit from these adaptive functionalities, including monitoring and accompanying rescue operations in highly variable physical environments, measuring environmental pollution in hazardous areas, or exploring natural environments where it is difficult to predict or pilot an exact route through unknown and changing terrains.

Due to the complexity of such scenarios, classic approaches of localization, mapping, and path planning require complex and heavy hardware and control systems (*54*, *55*) and will likely fail. We have demonstrated the feasibility and advantages of mimicking climbing plant behavior, enabling adaptive and autonomous decision-making in FiloBot. The plant-like behavioral control greatly simplifies sensing strategies and facilitates more agile information processing. Furthermore, it enables smaller dimensions and lower energy consumption. We also highlighted how additive manufacturing can be integrated with sensing and decision-making processes near the growing tip of the robot. This closely mimics how climbing plants can traverse complex environments adaptively by following simple rules. In biology, these represent the tropisms and growth dynamics that have evolved for a given environment. We have shown that such adaptive rules can be transferred to technical applications to reach autonomous and adaptive behaviors and enable, for example, environment navigation. Like plants in the natural world, 3D printer-based growing robots can use external cues to orient their movements. Like plants, they can grow towards light or against gravity and, therefore, use environmentally mediated behavior to navigate via movements directed by external signals. This strategy does not require specific path planning, visual feedback, or complex information processing but facilitates agility and ease of computation. In addition to the behaviors reported here, additional tropisms and movements exist in climbing plants that could be implemented to further enhance robot perception capabilities. Such mechanisms could include hydrotropism to follow, for example, underground water or humidity gradients and reach a water source in a given environment; thermotropism to locate heat sources; and chemotropism to identify and follow chemical traces in soil or gases in the air.

In the natural world, the journey from ground level to the tree canopy and unlimited light is probably constrained by available energy, particularly shade. Climbing plants fine-tune and economize energy by adjusting the amounts (and costs) of physiologically expensive mechanical tissues for mechanical support. When they need stiffness, they deposit thick-walled stiff tissue but develop “cheaper” less stiff material when safely attached.

Like climbing plants, the FiloBot uses embodied intelligence for its adaptive behaviors. It can tune the geometrical, physical, and mechanical properties of its body according to the physical constraints of different environments. It can develop stiffness to cross voids and then modify its material expenditure, forming less stiff stems when attached to supports.

FiloBot can also anchor to supports by twining around structures to climb vertically. When implemented around irregular structures, this growth habit helps the robot improve resistance to shear forces higher than its weight (Figure S5). This behavior reduces energy consumption and material costs compared to a purely self-supporting growth strategy. The robot can, therefore, morph its body characteristics according to the environment it travels through. This is another key attribute of the additive manufacturing robot we present here. Indeed, many climbing plants form strong interconnections between trees and other supports and eventually become physically part of the three-dimensional structure of the environment (*23*).

Finally, negotiating unpredictable terrains, particularly under real-world conditions, means that setbacks and malfunctions are probably inevitable. We have demonstrated that FiloBot can recover and re-direct growth following interruptions to the desired growth direction without a dedicated control for failure detection and task recovery.

Certainly, the robot differs from the natural model in several aspects. One important difference lies in the mechanical properties of its body, which must be defined during filament extrusion and cannot, unlike many plants, be modified following the initial growth phase. Plants can modify tissue properties over time (by aging), improving resistance of a basal part of the body during secondary growth. This dynamic adaptability allows plants to scale stiffness along their body and increase rigidity for tasks such as crossing voids or securing anchoring by thickening the stem when twining on supports. Additionally, using FDM generates some constraints as it is an intrinsically slow and irreversible process. However, a relatively slow robot movement might be beneficial in cluttered environments to avoid disturbing the surroundings, such as preventing proximal unstable objects or structures from collapsing. Similarly, retracting the robot from the environment might not necessarily be desired. In such cases, the use of biocompatible materials could be a good alternative to retain the robot where it was deployed and grew, thus acting as a new long-term structural element in the environment. Such uses can be envisaged, for instance, for reaching and monitoring tall trees and dense canopies, where the robot's growth process can serve as a stable support structure for further observations and data collection. Additionally, the robot could be deployed in compromised ecosystems using thermoplastic materials functionalized for phytoremediation (*56*). The robot's slow growth rate and ability to integrate into the environment make it well-suited for delicate ecological interventions without causing disruption.

We believe that by equipping autonomous systems with transportable additive manufacturing techniques merged with bioinspired behavioral strategies, future robots can be empowered to navigate unstructured and dynamic environments and even be capable of self-building infrastructures. We propose that basing soft robotic models on climbing plant growth has more to offer than basing a new design on a single specific mechanism and function. In fact, the consideration of diverse elements of the climbing plant growth strategies and the underlying development traits has a great potential for discovering new ways to improve robot functionalities. For a plant like robot these could include decision-making, economizing on materials, mimicing complex physiological adaptations with simple mechanical ones, providing safety and recovery from environmentally mediated mishaps, and thus interacting with the environment smartly and effectively.

MATERIALS AND METHODS

Robot design and fabrication

Filobot has a diameter of 40 mm, a volume of ≅ 42 cm^3, and weighs 82.5 g. It resulted in approximately 4/5 the diameter, 2/3 the area, and 1/2 the volume of the previous version. The reduced dimensions are intended to provide good maneuverability, energy efficiency, and efficient filament usage. Achieving this required a comprehensive rethinking of the entire design and fabrication process, building upon our previous experience (*6*, *9*, *57*). Refer to the Supplementary Materials for detailed comments about the scaling down and embodiment of additive manufacturing processes.

The FiloBot robotic head (Figure 5A) consists of a feeding mechanism and a plotting unit. The feeding mechanism pulls the incoming filament from the spooler through a DC motor and pushes it through a guiding tube toward the heater, which fuses the filament extruded from the nozzle (Figure 5B). The plotting unit rotates the robotic head through a gear connected to a second DC motor, resulting in a circular deposition of the extruded material. The robotic head is interfaced with the built body via four flexible clamping metal clips installed on the circumference. These clips prevent the rotation of the gear inside the printed body while allowing for axial sliding (Video S7).

The filament from the spooler passes inside the seed channel to the feeding channel and reaches the robotic head. When the feeding motor pulls the filament and the plotting starts to rotate. If not compensated, the filament accumulates torsion, creating kinking, knots, and eventually breakages. To counteract this torsion, we have adopted a passive mechanism that permits the spool to rotate freely in two axes, allowing the self-release of the filament without torsion (Figure 2A) (*9*). Such a passive mechanism works until the pulling force remains higher than the tension force experienced on the filament (see Supplementary Materials for an evaluation of the tension forces limiting displacement).

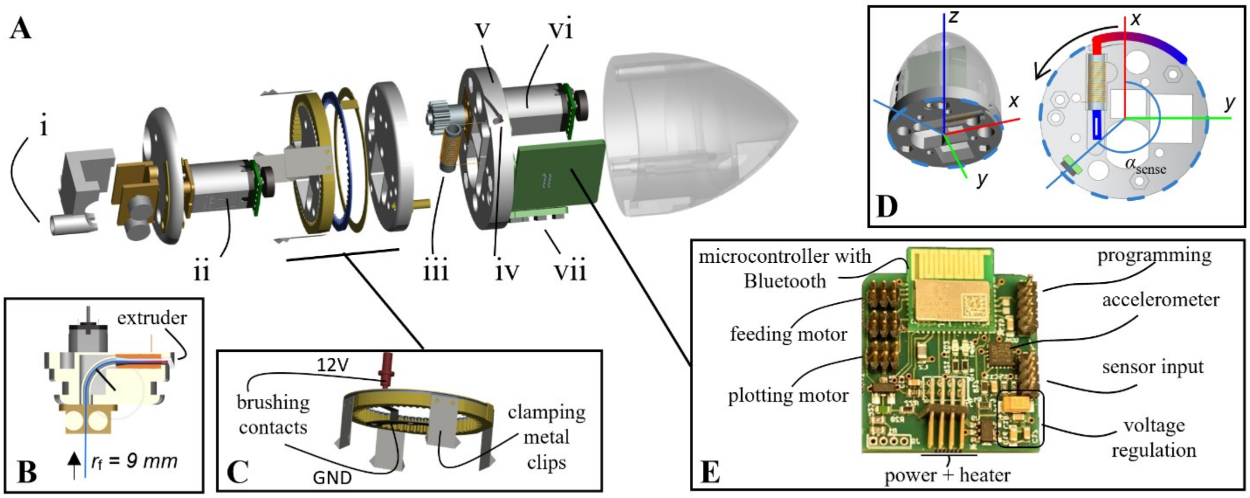

Fig. 5. FiloBot robotic head. (A) Exploded-view drawing of the FiloBot robotic head with: (i) feeding channel, (ii) feeding motor, (iii) heater, (iv) extruder, (v) plotting disk, (vi) plotting motor, and (vii) sensors board. **(B)** The internal section of the feeding channel showing the filament path. **(C)** The internal gear adapter anchors to the body structure through the clamping metal clips. In this way, it provides a pivot around which the growing mechanism rotates and, at the same time, implements an integrated slip ring for power transmission through brushing contacts. **(D)** Robot tip with its coordinate system, sensor position (at α_{sense}= 225° from the *x*-axis) and the plotting direction (black arrow). The material enters the heater in a solid and cold state (blue color in the picture), exits hot and malleable (red color), and solidifies again once deposited (gradient towards blue). The *x*-axis is aligned with the material deposition point. **(E)** The prototyped control board with an integrated Bluetooth link.

The robotic head comprises custom components, including four structural disks in polytetrafluoroethylene (PTFE) machined with a computer numerical control (CNC) tool, to host the mechanical and electronic components. The heater is a 14 mm long ceramic tube (outer diameter 4 mm, inner diameter 2 mm), machined from a ceramic block (MACOR® machinable ceramic) and wrapped with a Nickel/Chrome alloy wire with a diameter of 0.21 mm (RS PRO,714-1741) and a total resistance of 10 Ω. A 100 kΩ thermistor (EPCOS, B57540G0104J) is used to control the temperature of the heating coil. The feeding holder guides the filament into the feeding channel and anchors the feeding motor (gearbox GM12YN20-3DP 12V, Machifit) to the PTFE structure. The plotting geared mechanism consists of a commercial spur gear (RS PRO, 15 teeth, steel, module 0.5) coupled with the plotting motor (Pololu Corporation, 1000:1 Micro Metal Gearmotor HPCB 12V), which includes an embedded encoder (Pololu Corporation, Magnetic Encoder 12-CPR), and a custom slip ring.

The slip ring was CNC-machined from a commercial internal gear (Kyo Internal Gears IS50B60A-0350, module 0.5, reference diameter 30 mm) and used to accommodate the four metal clips (100 μm spring steel sheet brazed to the internal gear). The slip ring is a new component in this version that enhances the robot's robustness, serving both as an internal plotting gear and as a power transfer mechanism (Figure 5C). A brass ring was glued (Loctite 3450) on the internal gear to create a two-electrode pair for transferring power to the growing mechanism by two brushing contacts: one custom-made from a 0.1 mm spring steel sheet, the other by a spring-loaded pin (0850-0-15-20-83-14-11-0, Mill-Max Mfg. Corp.). Since it is anchored to the built structure through the clamping metal clips, the slip ring consents to confine the power lines along the side of the body from tip to base (Video

S7), avoiding twisting with the filament that moves centrally to the body following the plotter rotation (black arrow in Figure 5D).

The tip cover was 3D printed using nylon (ProX SLS 6100 by 3D Systems Inc.) and provided protection for the motors, the electronic board and sensors.

The board (Figure 5E and Figure S6) embeds an accelerometer (LIS331DLH from ST Microelectronics), a digital color sensor (VEML3328 from Vishay), and a microcontroller with an embedded transceiver module for Bluetooth Low Energy (CYBLE-014008-00 from Infineon/Cypress Semiconductor) to enable embedded control and communication with a PC for debugging purposes. The overall system architecture is shown in Figure S7, and the control architecture flowchart is reported in Figure S8.

The plotting components, including the plotting motor, were positioned inside the tip to limit mechanical interference between the parts and the grown structure. We placed most components into the tip to generate a distance from the heater, limiting the rise and diffusion of the temperature. Furthermore, internal disks and the external cover were pierced to facilitate airflow from inside the body to the outside. A cooling system composed of two fans was installed at the base to inject air into the body through two lateral channels (Figure 2A). We can set the air fans according to the environmental conditions and maintain the tip temperature below 65°C except for the heater location.

For the robot body, we chose Polylactic Acid (PLA) (Verbatim 55322), with a diameter of 1.75 mm. This was due to its fast-setting time, with a large difference between plotting – 170-190°C– and ambient –20-30°C– temperatures, and good mechanical properties that make it smooth during plotting with low material-tip friction and low stress on the plotting motor, as also being very robust after cooling. These features make PLA malleable and easily shapeable using tip motion and plotting control. See Table S5 for a qualitative comparison of commercial materials tested on the robot.

Relation between material deposition and control parameters

In our previous study (57), we achieved accurate material distribution and predictable bending by varying the plotting speed with a sinusoidal law. Specifically, the minimum speed corresponded to the point of maximum layer height, and the maximum speed corresponded to the minimum layer height. In the current implementation, we observed that the system could not achieve meaningful differential deposition on opposite sides of the circumference due to a shorter circumferential length. Varying heating temperatures could be a potential alternative to regulate the amount of material extruded. However, real-time temperature control during a deposition cycle of approximately 20 seconds with PLA thermal requirements is impractical. An alternative approach is to couple feeding (v_f) and plotting (v_p) speed control, which relates to the geometrical characteristics of the deposited layer (Figure 2E). The section area of a layer with a certain height $h(\alpha)$ and width $w(\alpha)$ at an angle α along the circumference can be expressed as:

$$S(\alpha) = h(\alpha)w(\alpha)\ [mm^2], \tag{17}$$

and computed as:

$$S(\alpha) = \frac{v_\mathrm{f}(\alpha)A}{v_\mathrm{p}(\alpha)}\ \ [mm^2], \tag{18}$$

where A is the spool filament section area. In our case, we have a nominal diameter of 1.75 mm. See Figure S1B for an experimental evaluation of layer section values. By substituting eq. (17) in eq. (18), the relationship between feeding speed, plotting speed, and deposited structure dimension can be obtained:

$$h(\alpha)w(\alpha) = \frac{v_\mathrm{f}(\alpha)A}{v_\mathrm{p}(\alpha)}. \tag{19}$$

The layer height for each deposition angle α can be modulated using (*57*):

$$h(\alpha) = -\frac{h_2 - h_1}{2}\cos(\alpha - \theta) + \frac{h_2 + h_1}{2}, \tag{20}$$

where θ is the bending direction, h_2 is the maximum layer height located at $\theta + \pi$, and h_1 is the layer minimum height located at θ.
The bending intensity I, experimentally found to be in the range $[0,0.4]$ (Figure S2), can be introduced to express h_1 as $(1 - I)h_2$. Upon this substitution, eq. (20) can be re-arranged into eq. (1). By knowing h_2 (setting as h from Table S1) and providing the bending intensity I, the height for each point in the circumference can be calculated.

Experimental settings and setups

Material deposition characterization. To verify the layer-by-layer adhesion and body construction, we tested multiple feeding, plotting, and temperature combinations in straight growth (Table S1). We varied the feeding speed linearly with respect to the plotting speed ($\overline{v}_{\mathrm{f}} = 3.5\overline{v}_{\mathrm{p}}$), keeping the extruded material always in tension to confine the filament under the plotting disk. To study the individual contribution of plotting and feeding in achieving a bending, we varied I_{f} and I_{p} in the range $[0,1]$ and experimentally defined I_{f} and I_{p} as functions of I for different temperatures (Table S2 and Figure S2).

Bending moment. Three structures with a length of 15 cm were tested for each combination of parameters. A 3-point bending test was performed using a Zwick-Roell Z050 tensile machine (load cell of 10kN), and the bending moment (M) obtained by,

$$M = \frac{WL}{4}, \tag{21}$$

with W the force at breakage (maximal force) and L the length of the specimen.

Twining. Filobot was located near a pole with a diameter of 7 cm and secured to a gripper positioned such that the robot's tip had a 50° inclination angle with respect to the horizontal plane.

Gravitropism. Filobot was attached to a gripper and positioned with its tip inclined at 45° with respect to the vertical axis (Figure 4A). After approximately 40 minutes of growth, the system was perturbed by rotating the gripper counterclockwise by approximately 90°.

Phototropism. Filobot was fixed to a gripper with its tip upward and aligned with the vertical axis. The experiment was conducted with various LED (Philips, 929002068299) and room light combinations. Figure S9A shows the arrangement of the scene.

Skototropism. Filobot was fixed to a gripper with its tip upward and aligned with the vertical axis. A green plant (*Ficus elastica* Roxb. ex Hornem.) was located approximately 24 cm from the robot's central tip to the trunk. A diffuse room light with a visible white spectrum was present in the scene, and a lamp (Philips, IR100C) was used to emit far-red light. Figure S9B shows the arrangement of the scene.

References and Notes

1. C. Laschi, B. Mazzolai, M. Cianchetti, Soft robotics: Technologies and systems pushing the boundaries of robot abilities. *Science Robotics*. **1**, eaah3690 (2016).

2. T. J. Wallin, J. Pikul, R. F. Shepherd, 3D printing of soft robotic systems. *Nat Rev Mater*. **3**, 84–100 (2018).

3. E. Del Dottore, A. Sadeghi, A. Mondini, V. Mattoli, B. Mazzolai, Toward Growing Robots: A Historical Evolution from Cellular to Plant-Inspired Robotics. *Frontiers in Robotics and AI*. **5** (2018), doi:10.3389/frobt.2018.00016.

4. H. Tsukagoshi, N. Arai, I. Kiryu, A. Kitagawa, Tip Growing Actuator with the Hose-Like Structure Aiming for Inspection on Narrow Terrain. *International Journal of Automation Technology*. **5**, 516–522 (2011).

5. E. W. Hawkes, L. H. Blumenschein, J. D. Greer, A. M. Okamura, A soft robot that navigates its environment through growth. *Science Robotics*. **2** (2017).

6. A. Sadeghi, A. Mondini, B. Mazzolai, Toward Self-Growing Soft Robots Inspired by Plant Roots and Based on Additive Manufacturing Technologies. *Soft Robotics*. **4**, 211–223 (2017).

7. N. D. Naclerio, A. Karsai, M. Murray-Cooper, Y. Ozkan-Aydin, E. Aydin, D. I. Goldman, E. W. Hawkes, Controlling subterranean forces enables a fast, steerable, burrowing soft robot. *Science Robotics*. **6**, eabe2922 (2021).

8. J. D. Greer, L. H. Blumenschein, R. Alterovitz, E. W. Hawkes, A. M. Okamura, Robust navigation of a soft growing robot by exploiting contact with the environment. *The International Journal of Robotics Research*. **39**, 1724–1738 (2020).

9. A. Sadeghi, E. Del Dottore, A. Mondini, B. Mazzolai, Passive Morphological Adaptation for Obstacle Avoidance in a Self-Growing Robot Produced by Additive Manufacturing. *Soft Robotics*. **7**, 85–94 (2020).

10. M. M. Hausladen, B. Zhao, M. S. Kubala, L. F. Francis, T. M. Kowalewski, C. J. Ellison, Synthetic growth by self-lubricated photopolymerization and extrusion inspired by plants and fungi. *Proceedings of the National Academy of Sciences*. **119**, e2201776119 (2022).

11. M. M. Coad, L. H. Blumenschein, S. Cutler, J. A. R. Zepeda, N. D. Naclerio, H. El-Hussieny, U. Mehmood, J.-H. Ryu, E. W. Hawkes, A. M. Okamura, Vine Robots: Design, Teleoperation, and Deployment for Navigation and Exploration. *IEEE Robotics Automation Magazine*. **27**, 120–132 (2020).

12. I. D. Walker, "Biologically inspired vine-like and tendril-like robots" in *2015 science and information conference (SAI)* (IEEE, 2015), pp. 714–720.

13. P. A. der Maur, B. Djambazi, Y. Haberthür, P. Hörmann, A. Kübler, M. Lustenberger, S. Sigrist, O. Vigen, J. Förster, F. Achermann, E. Hampp, R. K. Katzschmann, R. Siegwart, "RoBoa: Construction and Evaluation of a Steerable Vine Robot for Search and Rescue Applications" in *2021 IEEE 4th International Conference on Soft Robotics (RoboSoft)* (2021), pp. 15–20.

14. Y. Satake, A. Takanishi, H. Ishii, Novel growing robot with inflatable structure and heat-welding rotation mechanism. *IEEE/ASME Transactions on Mechatronics*. **25**, 1869–1877 (2020).

15. J. D. Greer, T. K. Morimoto, A. M. Okamura, E. W. Hawkes, A Soft, Steerable Continuum Robot That Grows via Tip Extension. *Soft Robotics*. **6**, 95–108 (2019).

16. S. K. Talas, B. A. Baydere, T. Altinsoy, C. Tutcu, E. Samur, Design and development of a growing pneumatic soft robot. *Soft Robotics*. **7**, 521–533 (2020).

17. T. Yan, S. Teshigawara, H. H. Asada, "Design of a growing robot inspired by plant growth" in *2019 IEEE/RSJ International Conference on Intelligent Robots and Systems (IROS)* (IEEE, 2019), pp. 8006–8011.

18. M. Kayser, L. Cai, S. Falcone, C. Bader, N. Inglessis, B. Darweesh, N. Oxman, FIBERBOTS: an autonomous swarm-based robotic system for digital fabrication of fiber-based composites. *Construction Robotics*. **2**, 67–79 (2018).

19. K. Zhang, P. Chermprayong, F. Xiao, D. Tzoumanikas, B. Dams, S. Kay, B. B. Kocer, A. Burns, L. Orr, C. Choi, D. D. Darekar, W. Li, S. Hirschmann, V. Soana, S. A. Ngah, S. Sareh, A. Choubey, L. Margheri, V. M. Pawar, R. J. Ball, C. Williams, P. Shepherd, S. Leutenegger, R. Stuart-Smith, M. Kovac, Aerial additive manufacturing with multiple autonomous robots. *Nature*. **609**, 709–717 (2022).

20. P. Rothemund, Y. Kim, R. H. Heisser, X. Zhao, R. F. Shepherd, C. Keplinger, Shaping the future of robotics through materials innovation. *Nat. Mater.* **20**, 1582–1587 (2021).

21. L. Cecchini, S. Mariani, M. Ronzan, A. Mondini, N. M. Pugno, B. Mazzolai, 4D Printing of Humidity-Driven Seed Inspired Soft Robots. *Advanced Science*. **10**, 2205146 (2023).

22. N. Rowe, S. Isnard, T. Speck, Diversity of mechanical architectures in climbing plants: an evolutionary perspective. *Journal of Plant Growth Regulation*. **23**, 108–128 (2004).

23. P. Soffiatti, E. Fort, C. Heinz, N. P. Rowe, Trellis-forming stems of a tropical liana Condylocarpon guianense (Apocynaceae): A plant-made safety net constructed by simple “start-stop” development. *Front. Plant Sci.* **13**, 1016195 (2022).

24. P. Soffiatti, N. P. Rowe, Mechanical Innovations of a Climbing Cactus: Functional Insights for a New Generation of Growing Robots. *Front. Robot. AI*. **7**, 64 (2020).

25. J. S. Mehling, M. A. Diftler, M. Chu, M. Valvo, "A minimally invasive tendril robot for in-space inspection" in *The First IEEE/RAS-EMBS International Conference on Biomedical Robotics and Biomechatronics, 2006. BioRob 2006.* (IEEE, 2006), pp. 690–695.

26. M. B. Wooten, I. D. Walker, "A novel vine-like robot for in-orbit inspection" in (45th International Conference on Environmental Systems, 2015).

27. M. B. Wooten, I. D. Walker, Vine-inspired continuum tendril robots and circumnutations. *Robotics*. **7**, 58 (2018).

28. M. Wooten, C. Frazelle, I. D. Walker, A. Kapadia, J. H. Lee, "Exploration and inspection with vine-inspired continuum robots" in *2018 IEEE International Conference on Robotics and Automation (ICRA)* (IEEE, 2018), pp. 5526–5533.

29. J. Gallentine, M. B. Wooten, M. Thielen, I. D. Walker, T. Speck, K. Niklas, Searching and Intertwining: Climbing Plants and GrowBots. *Front. Robot. AI*. **7**, 118 (2020).

30. B. Mazzolai, I. Walker, T. Speck, Editorial: Generation Growbots: Materials, Mechanisms, and Biomimetic Design for Growing Robots. *Frontiers in Robotics and AI*. **8** (2021), doi:10.3389/frobt.2021.711942.

31. I. Must, E. Sinibaldi, B. Mazzolai, A variable-stiffness tendril-like soft robot based on reversible osmotic actuation. *Nature Communications*. **10** (2019), doi:10.1038/s41467-018-08173-y.

32. T. Preuten, T. Hohm, S. Bergmann, C. Fankhauser, Defining the Site of Light Perception and Initiation of Phototropism in Arabidopsis. *Current Biology*. **23**, 1934–1938 (2013).

33. Y. Li, K. Swaminathan, M. E. Hudson, Rapid, Organ-Specific Transcriptional Responses to Light Regulate Photomorphogenic Development in Dicot Seedlings. *Plant Physiology*. **156**, 2124–2140 (2011).

34. H. Fukaki, M. Tasaka, Gravity perception and gravitropic response of inflorescence stems in Arabidopsis thaliana. *Advances in Space Research*. **24**, 763–770 (1999).

35. B. Moulia, E. Badel, R. Bastien, L. Duchemin, C. Eloy, The shaping of plant axes and crowns through tropisms and elasticity: an example of morphogenetic plasticity beyond the shoot apical meristem. *New Phytologist*. **233**, 2354–2379 (2022).

36. K. Yamamoto, T. Suzuki, Y. Aihara, K. Haga, T. Sakai, A. Nagatani, The Phototropic Response is Locally Regulated Within the Topmost Light-Responsive Region of the Arabidopsis thaliana Seedling. *Plant and Cell Physiology*. **55**, 497–506 (2014).

37. E. Gianoli, The behavioural ecology of climbing plants. *AoB plants*. **7** (2015).

38. T. Hattermann, L. Petit-Bagnard, C. Heinz, P. Heuret, N. P. Rowe, Mind the Gap: Reach and Mechanical Diversity of Searcher Shoots in Climbing Plants. *Front. For. Glob. Change*. **5**, 836247 (2022).

39. C. Darwin, *The movements and habits of climbing plants* (John Murray, 1875).

40. C. Darwin, F. Darwin, The power of movement in plants. (1883).

41. D. R. Strong, T. S. Ray, Host Tree Location Behavior of a Tropical Vine (Monstera gigantea) by Skototropism. *Science*. **190**, 804–806 (1975).

42. H. Smith, G. C. Whitelam, The shade avoidance syndrome: multiple responses mediated by multiple phytochromes. *Plant, Cell and Environment*. **20**, 840–844 (1997).

43. E. Del Dottore, A. Mondini, A. Sadeghi, B. Mazzolai, Characterization of the Growing From the Tip as Robot Locomotion Strategy. *Frontiers in Robotics and AI*. **6** (2019), doi:10.3389/frobt.2019.00045.

44. N. P. Rowe, T. Speck, "Stem biomechanics, strength of attachment, and developmental plasticity of vines and lianas" in *Ecology of Lianas*, S. A. Schnitzer, F. Bongers, R. J. Burnham, F. E. Putz, Eds. (John Wiley & Sons, Ltd, Chichester, UK, 2014; http://doi.wiley.com/10.1002/9781118392409.ch23), pp. 323–341.

45. S. Isnard, W. K. Silk, Moving with climbing plants from Charles Darwin's time into the 21st century. *American Journal of Botany*. **96**, 1205–1221 (2009).

46. S. Isnard, A. R. Cobb, N. M. Holbrook, M. Zwieniecki, J. Dumais, Tensioning the helix: A mechanism for force generation in twining plants. *Proceedings of the Royal Society B: Biological Sciences*. **276**, 2643–2650 (2009).

47. D. Kitazawa, Y. Hatakeda, M. Kamada, N. Fujii, Y. Miyazawa, A. Hoshino, S. Iida, H. Fukaki, M. T. Morita, M. Tasaka, H. Suge, H. Takahashi, Shoot circumnutation and winding movements require gravisensing cells. *Proc. Natl. Acad. Sci. U.S.A.* **102**, 18742–18747 (2005).

48. M. J. Correll, J. Z. Kiss, Interactions between gravitropism and phototropism in plants. *Journal of plant growth regulation*. **21** (2002).

49. B. Moulia, M. Fournier, The power and control of gravitropic movements in plants: a biomechanical and systems biology view. *Journal of Experimental Botany*. **60**, 461–486 (2009).

50. H. Chauvet, O. Pouliquen, Y. Forterre, V. Legué, B. Moulia, Inclination not force is sensed by plants during shoot gravitropism. *Sci Rep*. **6**, 35431 (2016).

51. W. R. Briggs, Phototropism: Some History, Some Puzzles, and a Look Ahead. *Plant Physiology*. **164**, 13–23 (2014).

52. E. Del Dottore, A. Mondini, B. Mazzolai, "Support localization strategy for growing robots aided by light perception inspired by climbing plants" in *2021 IEEE 4th International Conference on Soft Robotics (RoboSoft)* (IEEE, 2021), pp. 105–110.

53. E. Del Dottore, A. Mondini, A. Sadeghi, B. Mazzolai, Swarming behavior emerging from the uptake–kinetics feedback control in a plant-root-inspired robot. *Applied Sciences*. **8**, 47 (2018).

54. T. Taketomi, H. Uchiyama, S. Ikeda, Visual SLAM algorithms: a survey from 2010 to 2016. *IPSJ T Comput Vis Appl*. **9**, 16 (2017).

55. M. R. U. Saputra, A. Markham, N. Trigoni, Visual SLAM and Structure from Motion in Dynamic Environments: A Survey. *ACM Comput. Surv.* **51**, 1–36 (2019).

56. I. L. Liakos, A. Mondini, E. Del Dottore, C. Filippeschi, F. Pignatelli, B. Mazzolai, 3D printed composites from heat extruded polycaprolactone/sodium alginate filaments and their heavy metal adsorption properties. *Materials Chemistry Frontiers*. **4**, 2472–2483 (2020).

57. E. Del Dottore, A. Sadeghi, A. Mondini, B. Mazzolai, "Continuous growth in plant-inspired robots through 3D additive manufacturing" in *2018 IEEE International Conference on Robotics and Automation (ICRA)* (IEEE, 2018), pp. 3454–3460.

58. I. Gibson, D. W. Rosen, B. Stucker, M. Khorasani, *Additive manufacturing technologies* (Springer, 2021), vol. 17.

59. F. Calignano, D. Manfredi, E. P. Ambrosio, S. Biamino, M. Lombardi, E. Atzeni, A. Salmi, P. Minetola, L. Iuliano, P. Fino, Overview on Additive Manufacturing Technologies. *Proceedings of the IEEE*. **105**, 593–612 (2017).

60. E. Del Dottore, A. Mondini, A. Sadeghi, B. Mazzolai, "A plant-inspired kinematic model for growing robots" in *2018 IEEE International Conference on Soft Robotics (RoboSoft)* (IEEE, Livorno, 2018; https://ieeexplore.ieee.org/document/8404891/), pp. 20–24.

61. P. Vana, A. Alves Neto, J. Faigl, D. G. Macharet, "Minimal 3D Dubins Path with Bounded Curvature and Pitch Angle" in *2020 IEEE International Conference on Robotics and Automation (ICRA)* (IEEE, Paris, France, 2020; https://ieeexplore.ieee.org/document/9197084/), pp. 8497–8503.

62. A. Konyukhov, K. Schweizerhof, "Frictional Interaction of a Spiral Rope and a Cylinder – 3D-Generalization of the Euler-Eytelwein Formula Considering Pitch" in *Computational Contact Mechanics* (Springer Berlin Heidelberg, Berlin, Heidelberg, 2013; https://link.springer.com/10.1007/978-3-642-31531-2_14), vol. 67 of *Lecture Notes in Applied and Computational Mechanics*, pp. 413–422.

Acknowledgments: We thank Virgilio Mattoli for his continuous support during the research activities.

Funding: Supported by European Union’s Horizon 2020 Grant Agreement 824074 (GrowBot Project).

Author contributions: Conceptualization, Writing: EDD, AM, BM, NPR; Methodology, Software, Validation, Formal analysis, Investigation, Visualization: EDD, AM; Supervision, Funding acquisition: BM.

Competing interests: Authors declare that they have no competing interests.

Data and materials availability: All data needed to evaluate the conclusions in the paper are present in the paper or the Supplementary Materials. The datasets generated and analyzed in the current study are available at: https://gitlab.iit.it/EDelDottore/gb_filobot or at the Zenodo repository 10.5281/zenodo.10287323

https://www.science.org/doi/10.1126/scirobotics.adi5908

Supplementary Materials

Title: A growing soft robot with climbing plant inspired adaptive behaviors for navigation in unstructured environments

Authors:

Emanuela Del Dottore,[1]*† Alessio Mondini,[1]† Nick Rowe,[2] Barbara Mazzolai[1]*

Affiliations:

[1]Bioinspired Soft Robotics Lab, Fondazione Istituto Italiano di Tecnologia, Genova, Italy
[2] AMAP, Univ Montpellier, CIRAD, CNRS, INRAE, IRD, Montpellier, France

***Corresponding author(s): emanuela.deldottore@iit.it; barbara.mazzolai@iit.it**

† These authors contributed equally to this work

Supplementary Materials

Supplementary Methods
Supplementary Figures S1-S12
Supplementary Tables S1-S5
Supplementary Data file S1
Supplementary Videos S1-S8

Supplementary Methods

Considerations for the embodiment of additive manufacturing processes into robots. In growing robots based on additive manufacturing, the raw material must be transported from a base station to the moving robotic head to implement body mass increment from the tip. Among several alternatives (*58*), filaments have been selected as raw materials because they seemed more practical for upward growth. On the contrary, powder- or liquid-based methods, which require pressurized channels and not easily implementable material-state changing mechanisms, become complex and cumbersome. Fused Deposition Modeling (FDM) three-dimensional (3D) printers easily pull the filaments, which passively unroll from the spool, melting and printing the material in successive layers. FDM 3D printer components include a heated bed and an extruder, moving with a 3-axis slider, to deposit the filament following a 3D CAD model. Bed temperature, extruder temperature, plotting speed with the selected material, environmental temperature, and humidity are key parameters affecting printing quality. According to the adopted filament, extrusion temperatures range from about 100°C (with Polycaprolactone, PCL) to 175°C (with Polylactic acid, PLA) up to 400°C (with PolyEtherEtherKetone, PEEK). Each type of filament has its mechanical properties and requires *ad-hoc* printing parameters for the desired result (*59*). Printing parameters and the control strategy should be finely tuned for each operative environment of the robot.

When scaling down the concepts of FDM 3D printers for embodiment in growing robots, all the above aspects should be carefully considered at the design stage to ensure adequate performance, reliability, and good structural results given a selected raw material. For example, a small head diameter challenges the extruder dimensioning and the passage of the thermoplastic filament that must pass in narrow spaces with a possible high curvature. We had to find a compromise between filament curvature and extruder length. Too short extruder length limits the extrusion speed and, thus, the growth rate. Too high curvature instead stresses the feeding motor, especially for stiff filaments (Table S1). Here we use an extruder with a length of 14 mm and a resulting internal curvature of 9 mm (Figure 5D).

As mentioned above, the heating temperature is crucial to the overall system's performance. To a certain extent, high temperature in the plotting region might benefit good layer-to-layer adhesion (playing the role of the heated bed of classic 3D printers). However, if elevated temperatures persist, the structure becomes too soft and collapses (Figure S10), and motors slowly degrade. This issue is even more relevant considering the dimension of the robotic head that offers a small heat transfer surface.

Considerations on the growth speed. Additive manufacturing based on FDM is an intrinsically slow process and imposes constraints on the growth rate of the FiloBot. Material deposition in the robot is defined by three key parameters: extrusion temperature, feeding speed, and plotting speed. The feeding speed is critical in determining the extrusion rate and subsequent growth speed. Ideally, we can increase the growth speed by increasing the feeding speed. However, increasing the feeding speed reduces filament residence time in the heater, resulting in a lower material temperature upon extrusion and posing challenges for achieving layer adhesion.

We explored several strategies to ensure effective layer adhesion, including increasing the heater length, raising the heater temperature, or utilizing materials with lower melting temperatures. Considering the fixed system dimensions of 4 cm in our implementation, further meaningful optimization of the heater length proved to be challenging. Additionally, exceeding the current heater temperature of 200 °C could potentially harm the system (electronics and motors), despite the presence of a cooling system. Switching to alternative materials is viable, but it requires careful consideration. The ideal material should exhibit low friction to guarantee smooth plotting motion and possess sufficient stretchability to accommodate bending. However, a counter effect of low-melting materials is that their cooling time is prolonged, causing the material to remain in a soft state after deposition for a long period, potentially leading to high friction during plotting (e.g., as we experienced with PCL, Table S4) or generating structures that collapse.

Another potential approach to fasten growth involves employing 3 mm thermoplastic filaments. However, it implies scaling up the robot to use a larger motor and extruder, which contrasts with our goal to miniaturize the robot to gain maneuverability.

Conversion of unit measurements for motor speed. The plotting speed transforms from $x\left[\frac{°}{s}\right]$ to $y\left[\frac{\mathrm{mm}}{s}\right]$ as $y = \frac{xd\pi}{360}$, with d the diameter of the system, while the feeding speed transforms as $y = \frac{x r_{\mathrm{f}} \pi}{360}$, with $r_{\mathrm{f}} = 6.2[\mathrm{mm}]$ being the feeding gear diameter.

Comments about material deposition control. In FiloBot, the control law for differential material deposition proposed in (*57*) was not working properly because of the reduced circumferential length. The new design limits the sinusoidal law on the plotting speed in reaching its maximum and minimum expected velocities. That control needs a speed increment of the motor of more than five times its nominal speed, requiring a motor with a low gear ratio at the expense of the exercisable torque, which would then be insufficient for the rotation of the growing mechanism. An alternative could be to control the speed of the feeding motor alone. However, we needed to consider that the temperature of the extruded material changes with the feeding speed. The material passes rapidly from the heater when accelerating the feeding, remaining less melted. On the contrary, when reducing the feeding, the extrusion time slows down, causing the material to stay longer in the heater with a consequent over-melting. This condition leads to difficulties during extrusion: if the material is too soft, it accumulates in the heater and cannot be pulled out properly and plotted by the plotting motor rotation. This results in an irregular plot with holes and unwanted material accumulations along the structure.

For these reasons, controlling the single feeding or plotting speed does not ensure an effective differential deposition of the material.

Compensating for any variable times spent by the filament inside the heater via a control on the temperature is unfeasible because of the slow stabilization of this parameter with respect to motor speed.

Controlling plotting and feeding speed became necessary to ensure constant heating temperature on the extruded filament.

Kinematics and workspace evaluation. The forward kinematics of our robot can be described using the chain of homogenous transformation matrices over time ${}^{j}T = {}^{j}T_i T_i$ ($\in SO(4)$), as described in previous works (*43*, *60*). ${}^{j}T$ refers to a global reference frame j of the 3D environment where the robot moves, ${}^{j}T_i$ is the roto-transformation matrix from the local reference frame i to the global j, and T_i is the local roto-transformation matrix that controls the movement. In our system, T_i is described by the following matrix:

$$T_i = \begin{pmatrix} \cos^2(\theta+\pi)\cos\phi + \sin^2(\theta+\pi) & \cos(\theta+\pi)\sin(\theta+\pi)(\cos\phi - 1) & \cos(\theta+\pi)\sin\phi & -\frac{l\cos(\theta+\pi)(1-\cos\phi)}{\phi} \\ \cos(\theta+\pi)\sin(\theta+\pi)(\cos\phi - 1) & \cos^2(\theta+\pi) + \cos\phi\sin^2(\theta+\pi) & \sin(\theta+\pi)\sin\phi & -\frac{l\sin(\theta+\pi)(1-\cos\phi)}{\phi} \\ -\cos(\theta+\pi)\sin\phi & -\sin(\theta+\pi)\sin\phi & \cos\phi & \frac{l\sin\phi}{\phi} \\ 0 & 0 & 0 & 1 \end{pmatrix} \tag{22}$$

Here, l is the arclength for the growth step, and ϕ is the corresponding bending angle. ϕ is normalized between $[0, \bar{\phi}]$, where $\bar{\phi}$ is the maximal achievable bending angle due to curvature constraints $\bar{\phi} = l/r_\mathrm{c}$ and relates with the intensity I as in Figure S3B. The growth of the robot was simulated on MATLAB R2022b by implementing the kinematics model with the robot's update matrix in eq. (22). For the twining and environmentally mediated behaviors, θ and ϕ are obtained as described in corresponding sections above, and $l = G_\mathrm{s}\Delta t$, where Δt is the simulation time step and G_s is the growth speed. In our simulations, we set $\Delta t = 18$ s and $G_\mathrm{s} = 0.0041\frac{\mathrm{cm}}{s}$ if $\phi = 0$, or $G_\mathrm{s} = 0.0050\ \frac{\mathrm{cm}}{s}$ otherwise. These growth speeds were obtained experimentally on the robot (Table S2 and Table S3). G_s corresponds to control parameters $v_\mathrm{f} = 0.379\ \frac{\mathrm{cm}}{s}$ ($= \bar{v}_\mathrm{f}$ during bending), $v_\mathrm{p} = 20°/s$ ($= \bar{v}_\mathrm{p}$ during bending), and a heater temperature of 150°C during straight growth.

Theoretically, ${}^{j}T = {}^{j}T_i T_i$ ($\in SO(4)$) provides the position of the robot head in space, and this information can be used in a classic path-planning strategy (*43*). By knowing the starting and target positions in a 3D space and considering the curvature constraint, we can find the shortest path to reach the target with a 3D Dubin algorithm. For evaluating the workspace, 420 paths are generated with the minimum path algorithm provided with (*61*). Initial positions are always set to (0, 0, 0) with a 0° heading angle. Two curvature constraints are set for comparison: 8 cm, corresponding to the robot proposed in this paper, and 10 cm, corresponding to the robot developed in (*6*). No constraints are set to the pitch angle. Multiple distances are tested between starting and target positions (20, 60, 120 cm), each with multiple target headings (from 0° to 180° with a step of 45°). The 3D paths are generated with the Julia code modified from (*61*), exported as CSV files, and imported in a MATLAB script to generate the sequence of triples $\langle\theta, \phi, l\rangle$ used by the robot in simulation (*43*). All the tested combinations are available at the GitLab repository https://gitlab.iit.it/EDelDottore/gb_filobot. Comparing the performance of the two robots (Video S8 shows an example), we can highlight improved maneuverability (from 10 cm to 8 cm of r_c) leading to reduced paths length (up to ~20% less) needed to move from two arbitrary points in a 3D space, with a consequent reduced need for raw material (~40% less in entirely straight paths, up to ~60% with curves) and reduced energy expenditure (~0.6 times less) (Figure S11 and Table S4). However, errors accumulate and in long paths ${}^{j}T$ cannot provide a good approximation of the robot's position. The errors are generated first by the unpredictability of the environment, which might offer unforeseen obstacles inducing deviations from the expected path (*9*). Because of multiple factors affecting the printing (see "Considerations for the embodiment of additive manufacturing processes into robots"), the perfect alignment of successive layers cannot be ensured. Lastly, the robotic head also shows a slow, non-constant drifting in the rotation of the deposition head over time (~245 ± 40 °/h, Figure S12). Possibilities to correct these errors account for a complexification of the robot on both hardware and control (*54*, *55*). To preserve reduced dimensions, simplicity of sensing strategy, and agile information processing, we evaluated and demonstrated the feasibility of mimicking climbing plant behaviors for adaptive navigation in unstructured environments of growing robots.

Determining the gravity position in the robot's coordinate frame. The rotation of the tip (α_{r}) with respect to gravity can be calculated from the accelerometer. However, the data obtained from the accelerometer can be noisy due to vibrations from the motors and cooling fans. Therefore, we introduced a filter to calculate the difference between the plotting angle provided by the motor encoder (α_{m}) and α_{r}. Averaging this difference over a full plotting rotation, we obtain:

$$\Delta\alpha = \frac{\sum_1^N(\alpha_{\mathrm{m}}-\alpha_{\mathrm{r}})}{N}, \tag{23}$$

where N is the number of samples in one rotation. The current plotting angle (α) can then be obtained as:

$$\alpha = \alpha_{\mathrm{m}} - \Delta\alpha - \alpha_{\mathrm{ext}}. \tag{24}$$

Here, α_{ext} represents the relative position of the material deposition point with respect to the accelerometer x-axis. In our case, $\alpha_{\mathrm{ext}} = 0$, as the accelerometer is aligned with the deposition point. The gravity position (α_{g}) in the local reference system of the robot is determined by finding the absolute minimum value of α over one cycle. This value is $\cong 0$ when the tip is horizontal and the deposition point is directed downward, perpendicular to the ground.

Growth limits due to tension forces on the filament in curvilinear paths. When growing in curvilinear paths, the thermoplastic material can interact with the internal surface of the grown body structure and slide on it. This results in a friction force that opposes the pulling force (T_{hold}) actuated by the feeding motor at the robot head and contributes to defining a tension force (T_{load}) that the robot must counteract. If the body path is straight, the filament remains at the center of the body, thus, the frictional force does not act. In helical paths or turns, the tension force can grow exponentially with the increasing of the curve incremental angle (φ) and the friction value (μ) as defined by the Capstan equation:

$$T_{\mathrm{load}} = T_{\mathrm{hold}} e^{\mu\varphi}. \tag{25}$$

In our implementation:

- T_{load} is the tension exerted by the feeding motor, and at maximum power, it has a maximum force of 11.2 ± 0.3 N. To extract this value, we clamped the filament to a load cell and locked the other extremity into the growing robot. We averaged five pulling tests. The value we found is lower than the tensile force the PLA filament can withstand. We performed five tensile tests on 10 cm PLA filament samples and found a resistance of 120.5 ± 1.3 N. This means that no breakages can occur while the robot pulls the filament while growing.
- T_{hold} is the tension exerted by the spool necessary to unroll the filament. This is typically low because of the low friction gained by the bearings. However, due to the stiffness of the PLA filament and the torsion that can accumulate during unrolling, there might be occasional peaks in the resisting force. We performed five pulling tests, unrolling the filament with a load cell for 50 cm each from a spool at about half of its initial amount of material (initially, the spool has 1 kg of filament). The average peak force was 0.23 ± 0.08 N. The force peak depends on the amount of filament left in the spool: with a new spool, the filament has low curvature, and

the force perceived is lower, while in the last wraps, the filament has a high curvature that requires more force to unroll.

- μ is the friction coefficient equal to 0.46 ± 0.05 in our case. We averaged five measurements taken from five different grown structures, sliding a 2 cm filament over the inner surface of each structure.

Substituting our numbers in eq. (25), we obtain that the maximum curve that can be achieved before the feeding motor stops due to excessive tension is:

$$\varphi = \frac{1}{\mu} \ln \frac{T_{\text{load}}}{T_{\text{hold}}} = 8.45 = 2.68\,\pi \tag{26}$$

that corresponds to 1.34 turns.

This theorem, also known as the Euler-Eytelwein problem of a rope sliding over a cylinder, has been extended to spiral paths (*62*). The study by (*62*) demonstrated that, in the case of helical rolling, the load force depends on the radius and pitch of the spiral, and it decreases with an increase in pitch. Therefore, we can anticipate that FiloBot will be capable of performing longer paths in twining behavior when a larger pitch is implemented.

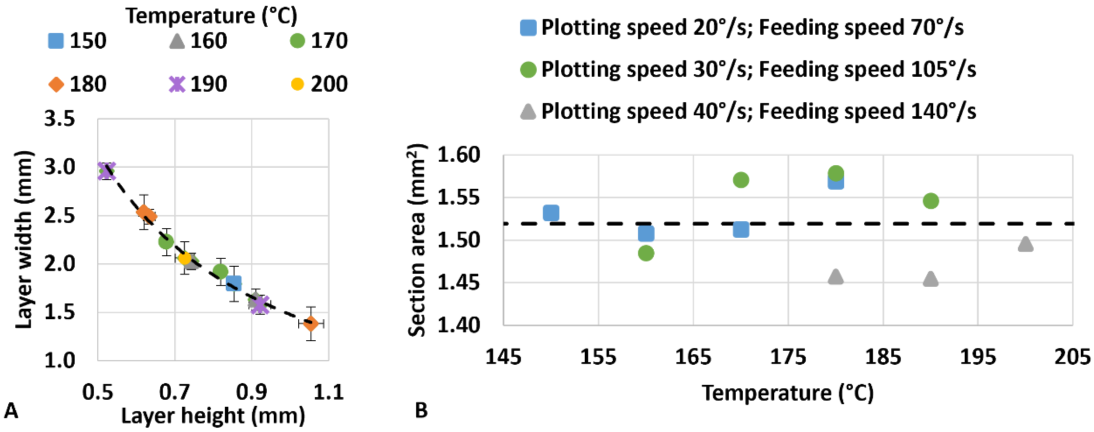

Fig. S 1. Results of different printing parameters. (A) Relation between layer height and width. In constant printing parameters (but variable values of temperature, feeding, and plotting speed), the body structure will be formed by almost constant layers and width (w) relates to height (h) with the law $w = 1.48h^{-1.1}$. **(B)** Obtained layer section area (dot data) and estimated average (dashed line) over different plotting and feeding speeds and temperatures.

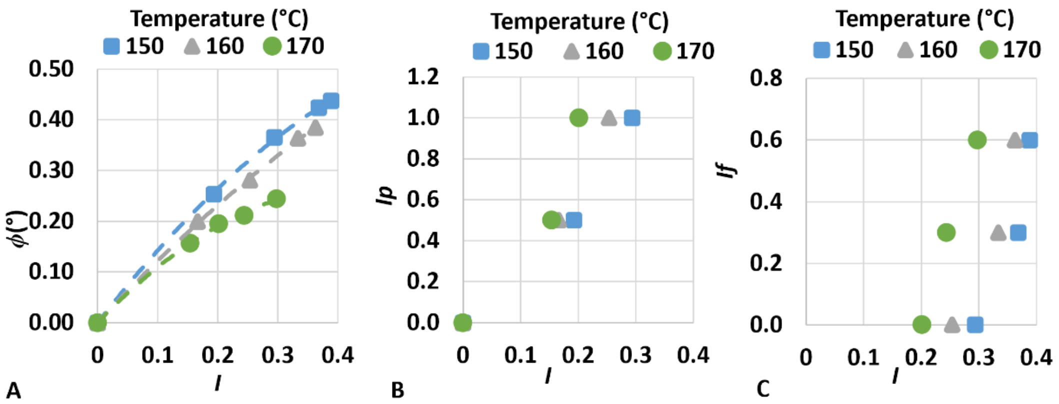

Fig. S 2. Bending intensity. (A) Experimental relationship established between the provided magnitude of intensity I and the achieved bending angle ϕ. Experimental results obtained for I providing different values to **(B)** I_{p} and **(C)** I_{f}. Tests are performed at three different temperatures with minimum plotting speed set to $\overline{v_{\mathrm{p}}} =$ 20°/s and maximal feeding speed to $\overline{v}_{\mathrm{f}} =$ 70°/s. The resulting functions are: at 150°C, $I_{\mathrm{f}} = 5.72I - 1.7$ and $I_{\mathrm{p}} = 8.05I^2 + 1.04I$; at 160°C, $I_{\mathrm{f}} = 5.13I - 1.3$ and $I_{\mathrm{p}} = 10.7I^2 + 1.22I$; at 170°C, $I_{\mathrm{f}} = 6.17I - 1.2$ and $I_{\mathrm{p}} = 21I^2 + 0.8I$; with cut-off functions to set $I_{\mathrm{f}} \in [0,0.6]$ and $I_{\mathrm{p}} \in [0,1]$.

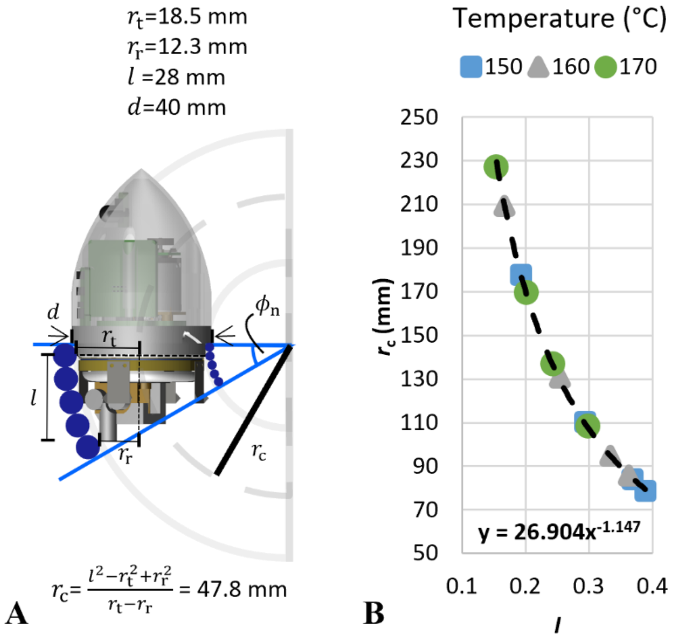

Fig. S 3. Curvature radius analysis. (A) Geometrical parameters defining the limit of the curvature radius imposed by mechanics. **(B)** Curvature radius values found experimentally on the robot. Tests are performed at three different temperatures with minimum plotting speed set to $\overline{v_p}$ = 20°/s and maximal feeding speed to $\overline{v}_f$ = 70°/s. In this configuration, the curvature radius relates to the intensity as $r_c \cong 26.9I^{-1.1}$.

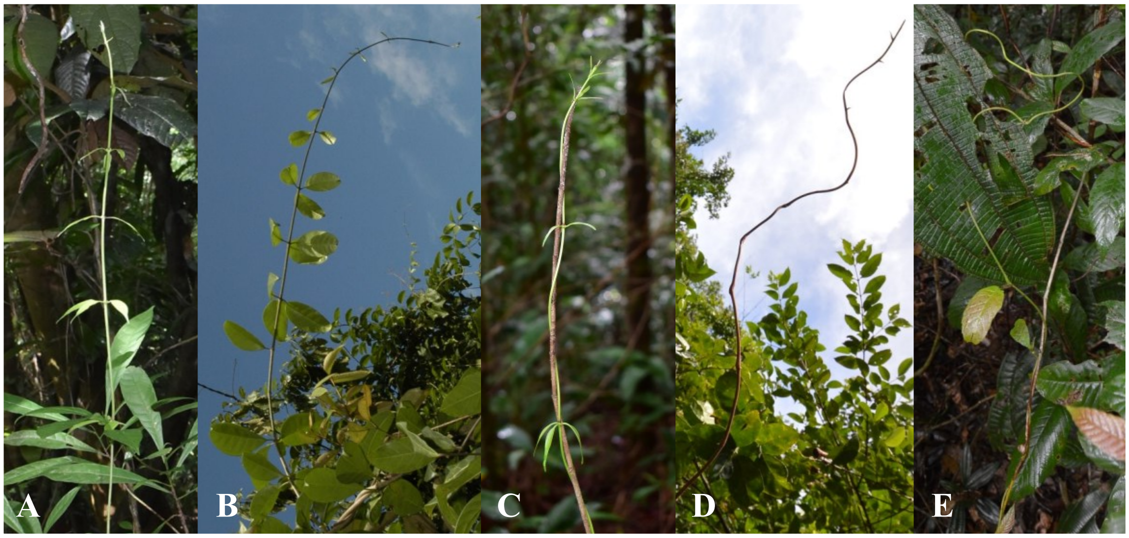

Fig. S 4. Range of adaptive growth behaviors in plants. (A) Straight **(B)** Bending, **(C)** Twining, **(D)** Arbitrary (considered in the FiloBot control architecture, Fig. S8). **(E)** Complex changes in adaptive behavior (twining below – arbitrary above) seen in climbing plants is a principal goal for safely navigating complex terrains via adaptive growth and even self-building infrastructures (Fig. 1E).

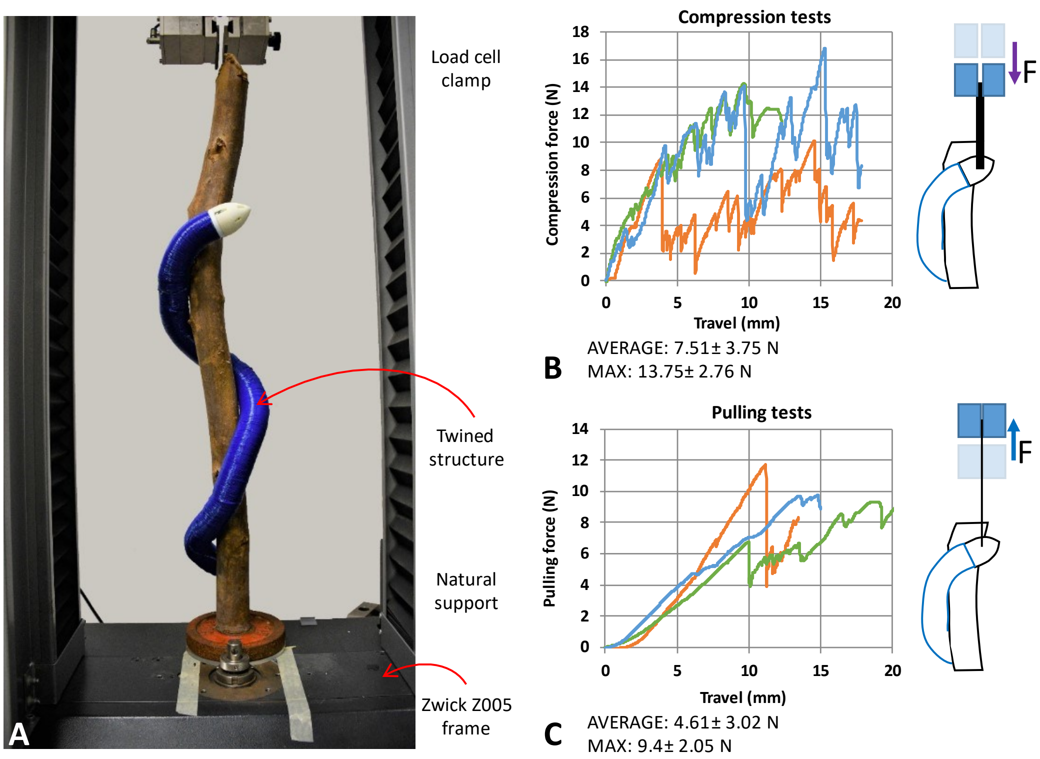

Fig. S 5. Anchoring force generated through twining. The twining behavior acts to anchor the robot to a supporting structure. If the structure has a seamless irregular shape, like a tree branch, the robot is secured against vertical sliding. **(A)** The testing setup includes a Universal Testing Machine to which the robot is attached through a thread (in pulling tests) and a rigid link (in compression tests). The robot is twined around a natural support and is free at the base. The natural support is anchored at the bottom with a 2 kg weight. The weight of the robot tip plus the body used in these tests is 2.85 N. **(B)** Compression and **(C)** pulling tests are conducted with three repetitions each, every time the body is rearranged differently around the branch. We needed up to 9.4 ± 2.05 N to pull the structure out and up to 13.7 ± 2.76 N before sliding during compression. Results show that the twining as performed by our robot is an anchoring strategy enabling the twined robot to sustain five times more than its weight in these tests. In the figure, the average is evaluated for the three samples over the entire displacement, and max is the average of the three peaks.

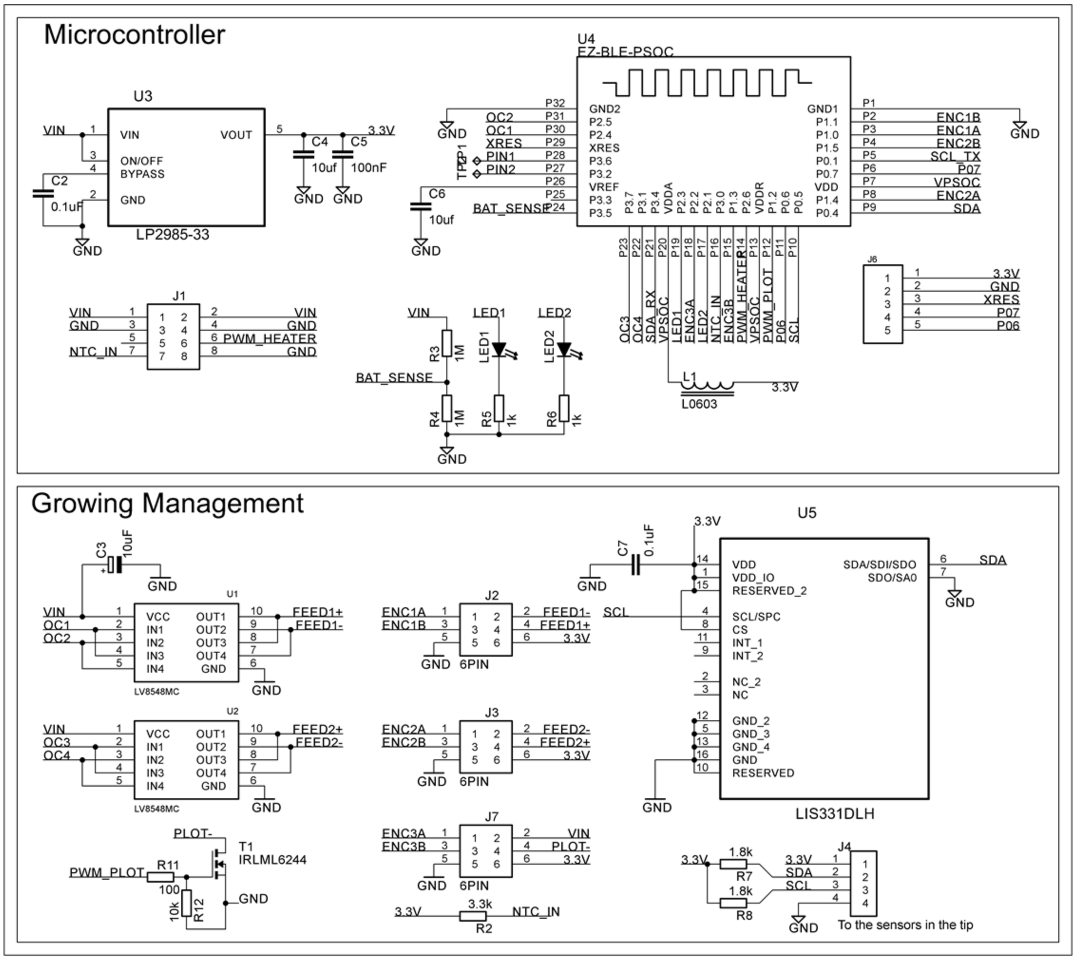

Fig. S 6. Schematics of the control board. A compact control board has been developed to fit into the growing head and manage its functionalities. The board controls the feeding and plotting motors through two motor drivers (LV8548MC from OnSemiconductor) and their respective quadrature magnetic encoders (Magnetic Encoder for Micro Metal Gearmotors from Pololu); the heater coil through a Mosfet (IRLML6244TR from Infineon); an accelerometer (LIS331DLH from ST Microelectronics); an I2C port for the connection of a digital color sensor integrated into the sensorized tip (VEML3328 from Vishay); two LEDs for robot states visualization.

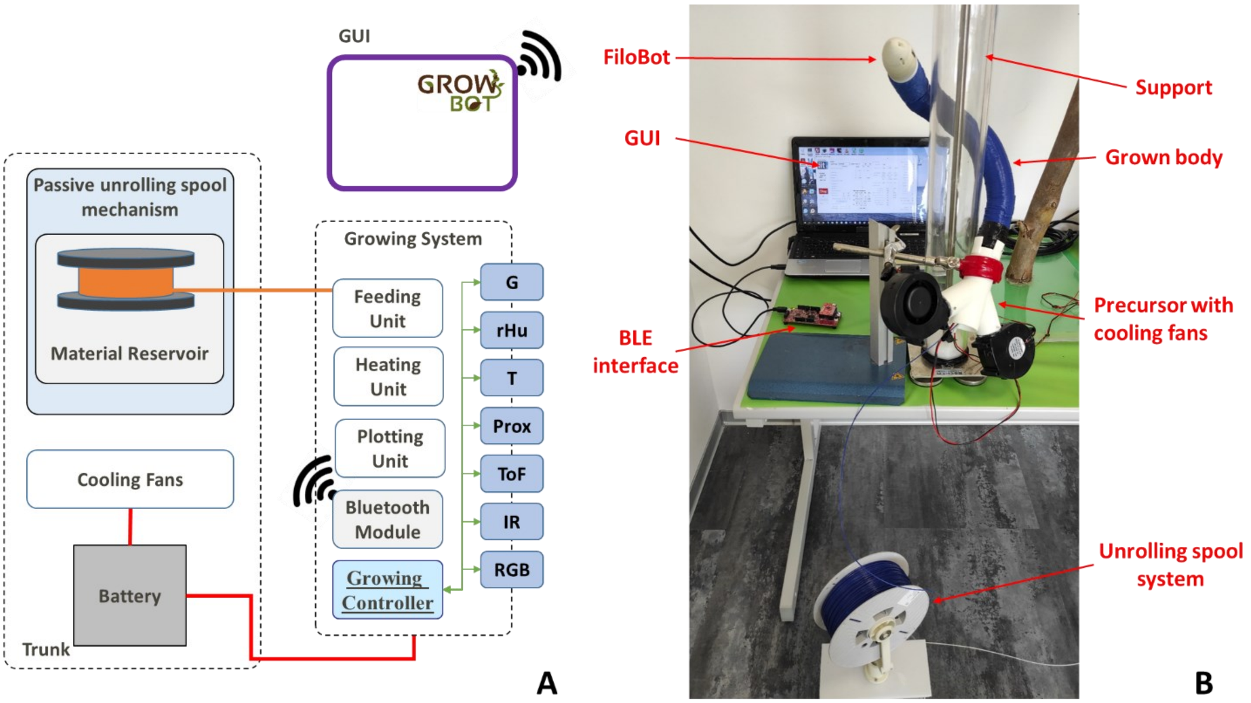

Fig. S 7. FiloBot architecture. (**A**) main components of the growing system and (**B**) typical experimental setup to perform growth experiments. It includes the apically growing mechanism (FiloBot) connected to a preprinted precursor via the grown body structure. This hosts the cooling fans and power lines, allowing the 3D printing filament to pass toward the head. The filament is fed from the spool mechanism below that releases the growing material passively. The robot is connected wirelessly to a Bluetooth interface and then to a custom Graphical User Interface developed in Visual Studio 2017 for debugging the robot and monitoring its data.

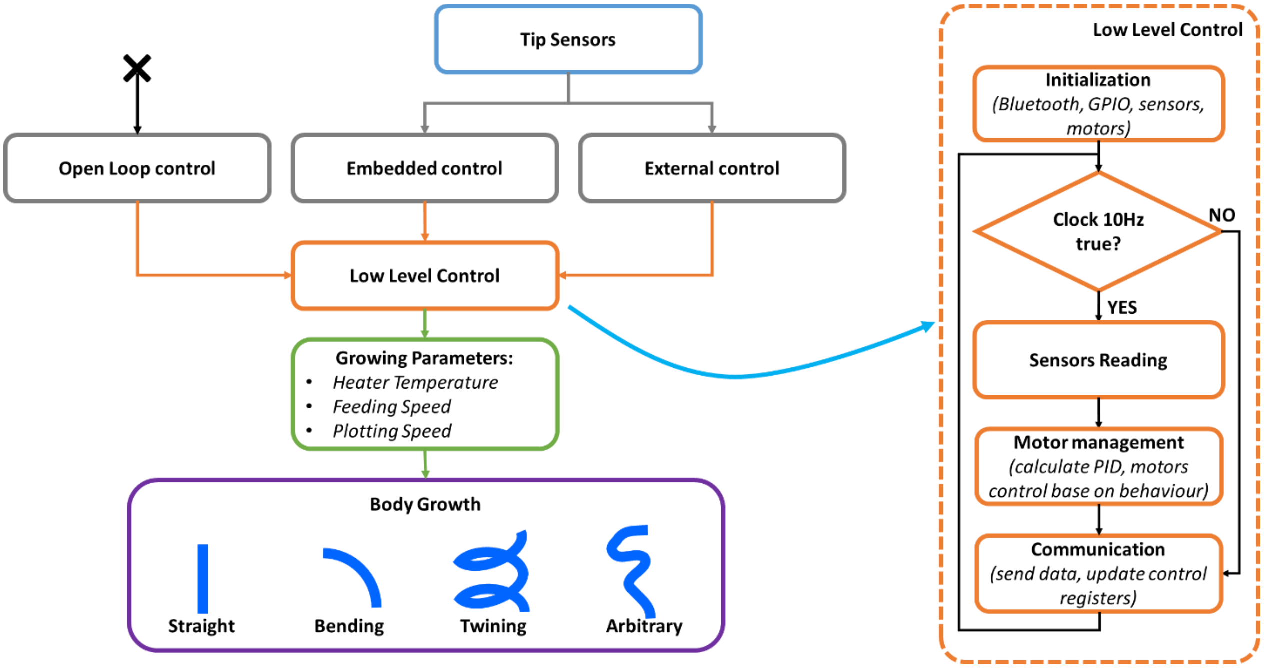

Fig. S 8. Flowchart of the control architecture. The growth can be controlled through the feeding speed, plotting speed, and heating temperature. By managing these parameters, it is possible to realize a structure with an almost arbitrary shape. The robot can set these parameters through the embedded control (see section "Environmentally mediated behaviors for robot navigation" in the main text), or a user can set them through an external interface that visualizes the sensors data and provides the commands for either an open-loop control on the motors or the possibility to set direction and intensity of an external (virtual) stimulus (external control in the chart). An embedded low-level control loop performs data acquisition, motors and heater management, and communication at 10 Hz.

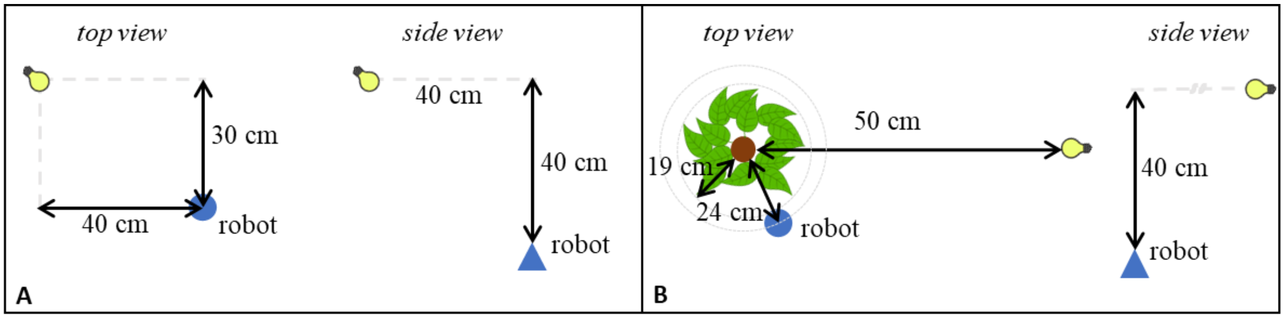

Fig. S 9. Scene settings for phototropism and skototropism. Distances for the objects used during (A) phototropic and (B) skototropic tests with the robot. Distances are considered with respect to the initial position of the robot tip.

Fig. S 10. Example of a collapsing body structure. Due to the high temperature (> 50 °C) in the tubular body, PLA does not solidify properly and remains soft, leading to the body's collapse during growth if not properly cooled. The result is a tubular body with a variable diameter, which also does not guarantee proper anchoring to the flexible internal clips, causing an irregular deposition.

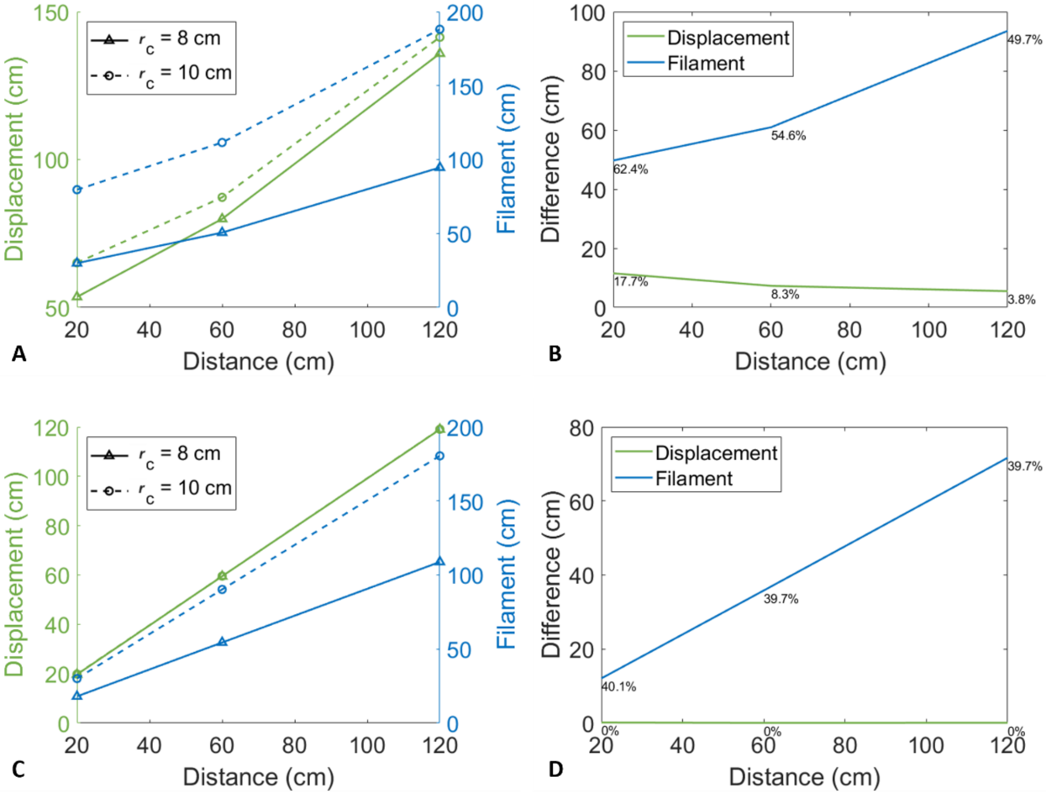

Fig. S 11. Performance comparison between robots having r_c=8 cm and r_c=10 cm. **(A)** Averaged displacement and filament consumption obtained over 420 paths generated in 3D. **(B)** Evaluation of the performance difference between the two robots. The new design uses up to 60% less filament, and shortest paths are achieved with the highest gain in short distances. **(C)** Averaged displacement and filament consumption obtained in straight growths. **(D)** Evaluation of the performance difference between the two robots: 40% less filament is used with the new design.

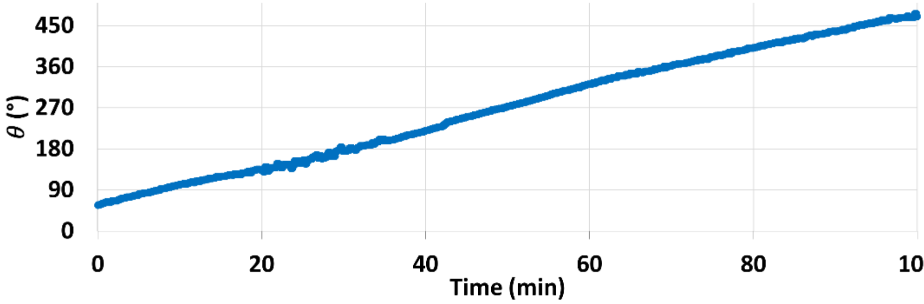

Fig. S 12. A characteristic drift of the tip. The robot is bending in a plane. The deposition angle shifts over time due to tip slippages.

Table S1. Deposition of material in straight growth. Multiple combinations of temperature, plotting, and feeding speed have been tested, which produced different layer thicknesses and widths. The expected surface area is calculated from the obtained layer parameters.

Temperature [°C]	**Layer Thickness (*h*) [mm]**		**Layer Width (*w*) [mm]**		**Surface Area [mm^2]**	**Speed in 1 layer [s]**	**Growth speed [mm/s]**
	AVG	**STDEV**	**AVG**	**STDEV**	***h·w***		
$\overline{v}_p$ = 20°/s; $\overline{v}_f$ = 70°/s						18	
150	0.8543	0.0178	1.7933	0.1806	1.5321		**0.0475**
160	0.7432	0.0101	2.0292	0.0847	1.5080		**0.0413**
170	0.6787	0.0134	2.2292	0.1408	1.5129		**0.0377**
180	0.6192	0.0133	2.5342	0.1816	1.5691		**0.0344**
$\overline{v}_p$ = 30°/s; $\overline{v}_f$ = 105°/s						12	
160	0.9106	0.0165	1.6308	0.1093	1.4851		**0.0759**
170	0.8193	0.0125	1.9175	0.1413	1.5711		**0.0683**
180	0.6339	0.0151	2.4908	0.0771	1.5790		**0.0528**
190	0.5226	0.0129	2.9592	0.0890	1.5465		**0.0436**
$\overline{v}_p$ = 40°/s; $\overline{v}_f$ = 140°/s						9	
180	1.0541	0.0324	1.3825	0.1731	1.4573		**0.1171**
190	0.9217	0.0282	1.5783	0.0962	1.4547		**0.1024**
200	0.7258	0.0249	2.0608	0.1678	1.4957		**0.0806**

Table S2. Deposition of material during bending. Multiple combinations of temperature, I_f and I_p have been tested with $\overline{v_\mathrm{p}}$ = 20°/s and $\overline{v}_\mathrm{f}$ = 70°/s in eq. (2) and (3). Five samples of ten layers were realized for each combination of plotting parameters. The total height for the ten layers was measured with a caliper on the sides of maximum and minimum deposition and divided by 10 to get the single-layer heights. The obtained minimum h_1 and maximum h_2 height is reported in the table, with the corresponding growth velocities having a speed in one deposition cycle during bending of 12 s (Table S1). $I = \frac{h_2 - h_1}{h_2}$, $r_\mathrm{c} = \frac{d}{2}\frac{h_2 + h_1}{h_2 - h_1}$, $k = \frac{1}{r_\mathrm{c}}$ and ϕ is obtained from the curve fitting (Figure S2): for 170 °C $\phi = -1.4002 I^2 + 1.2288 I + 0.0002$, for 160 °C $\phi = -0.5659 I^2 + 1.2663 I + 0.0005$ and for 150 °C $\phi = -1.026 I^2 + 1.5297 I + 0.0006$

Temperature [°C]	I_f	I_p	h_1 **[mm]**	**STDEV**	h_2 **[mm]**	**STDEV**	**Growth speed [mm/s]**	r_c **[mm]**	k	I	ϕ **[°]**
170	0	0	0.6787	0.0134	0.6787	0.0134	0.0377			0	0
170	0	0.5	0.5700	0.0140	0.6740	0.0145	0.0518	227	0.2521	0.1543	0.1565
170	0	1	0.5110	0.0114	0.6400	0.0082	0.0480	170	0.3380	0.2016	0.1910
170	0.3	1	0.4340	0.0232	0.5740	0.0122	0.0420	137	0.4188	0.2439	0.2166
170	0.6	1	0.3810	0.0162	0.5430	0.0135	0.0385	108	0.5287	0.2983	0.2422
160	0	0	0.7432	0.0101	0.7432	0.0101	0.0413			0	0
160	0	0.5	0.6610	0.0122	0.7930	0.0145	0.0606	209	0.2738	0.1665	0.1950
160	0	1	0.5470	0.0157	0.7330	0.0122	0.0533	131	0.4382	0.2538	0.2848
160	0.3	1	0.4810	0.0161	0.7220	0.0104	0.0501	95	0.6041	0.3338	0.3595
160	0.6	1	0.4480	0.0157	0.7030	0.0162	0.0480	86	0.6681	0.3627	0.3848
150	0	0	0.8543	0.0178	0.8543	0.0178	0.0475			0	0
150	0	0.5	0.7020	0.0166	0.8700	0.0084	0.0655	178	0.3223	0.1931	0.2565
150	0	1	0.5810	0.0087	0.8230	0.0099	0.0585	110	0.5198	0.2940	0.3605
150	0.3	1	0.4820	0.0148	0.7630	0.0125	0.0519	84	0.6806	0.3683	0.4236
150	0.6	1	0.4560	0.0184	0.7460	0.0223	0.0501	79	0.7275	0.3887	0.4390

Table S3. Theoretical extension along voids and Young's modulus of the structures. From the obtained bending moments, we can estimate the maximum straight path the robot can theoretically perform horizontally for each combination of parameters. Knowing the tip weight ($w_{\mathrm{t}} = 84g$) and an average weight of the structure ($w_{\mathrm{e}} = 10\,\frac{g}{\mathrm{cm}}$) in a unit length, we can rewrite the relation of the bending moment $M = \frac{WL}{4}$ found with the 3-point bending test into $M = \frac{L^2 w_{\mathrm{e}}}{2} + L w_{\mathrm{t}}$, where $L w_{\mathrm{t}}$ is the bending moment of a beam of length L, with one extremity fixed and a load at its free extremity, and $\frac{L^2 w_{\mathrm{e}}}{2}$ is the bending moment of a beam fixed at one extremity with a distributed load per unit length (w_{e}). By solving the equation ($\frac{w_{\mathrm{e}}}{2} L^2 + w_{\mathrm{t}} L - M = 0$) for L, we find possible extensions ranging from ~1 m to ~6 m. These lengths should be rescaled if additional loads have to be carried. The last columns presents the corresponding Young's modulus of the structures.

Temperature (°C)	$\overline{v_{\mathrm{p}}}$ **(°/s)**	$\overline{v}_{\mathrm{f}}$ **(°/s)**	**Bending moment *M* (avg ±std, Nm)**	**Suspended body length *L* (m)**	**Young's modulus (GPa)**
150	20	70	3.88 ±1.76	1.47	0.055±0.007
160	20	70	7.024 ±3.92	2.08	0.069±0.009
170	20	70	14.608 ±4.17	3.13	0.084±0.014
180	20	70	31.453 ±7.54	4.74	0.148±0.027
160	30	105	7.414 ±3.98	2.15	0.098±0.025
170	30	105	13.078 ±3.23	2.95	0.152±0.016
180	30	105	29.81 ±8.45	4.61	0.262±0.021
190	30	105	57 ±6.51	6.49	0.515±0.049
180	40	140	3.751 ±2.18	1.45	0.065±0.015
190	40	140	8.68 ±4.78	2.35	0.086±0.024
200	40	140	13.46 ±2.72	2.99	0.133±0.042

Table S4. Power consumption with various printing parameters. Estimated power consumption given different printing parameters and in straight growth for the growing robot developed here. To estimate consumption during a turn with minimum curvature radius, we recall that it is obtained at 150°C, $\overline{v_p}$ = 20°/s, and $\overline{v_f}$ = 70°/s = 3.79 mm/s with a growth speed of 0.05 mm/s, leading to 151 J to growth 1 mm. In a previous implementation (*6*), the growing robot consumed ~14 W. Considering a growth speed of 0.053 mm/s at 190°C, $\overline{v_p}$ = 20°/s and feeding speed of 8 mm/s, used to reach its minimum curvature radius (*57*), the energy expenditure reached 250 J to grow 1 mm while performing a turn.

	T[°C]	I[A]	Power Growing System [W]	Power Cooling System [W]	Total [W]	Time to growth 1 mm [s]	Energy for 1 mm growth [J]
$\overline{v_p}$ = 20°/s $\overline{v_f}$ = 70°/s	180	0.74	8.88	3.53	12.41	29.07	258.15
	170	0.71	8.52	3.53	12.05	26.52	225.96
	160	0.66	7.92	3.53	11.45	24.22	191.83
	150	0.63	7.56	3.53	11.09	21.07	159.28
$\overline{v_p}$ = 30°/s $\overline{v_f}$ = 105°/s	190	0.97	11.64	3.53	15.17	22.96	267.28
	180	0.94	11.28	3.53	14.81	18.93	213.53
	170	0.89	10.68	3.53	14.21	14.65	156.42
	160	0.86	10.32	3.53	13.85	13.18	135.99
$\overline{v_p}$ = 30°/s $\overline{v_f}$=105°/s	200	1.18	14.16	3.53	17.69	12.40	175.59
	190	1.12	13.44	3.53	16.97	9.76	131.24
	180	1.08	12.96	3.53	16.49	8.54	110.65

Table S5. Features of FDM 3D printable materials. Analysis of benefits and drawbacks of different 3D printable, commercially available materials tested on the growing robot to measure the system's compatibility.

Material	Pro	Cons
Polylactic acid - PLA	Very smooth material during the deposition. It solidifies very quickly, ensuring low friction. The material is biodegradable.	The filament is relatively stiff, which causes stress to the feeding motor. The deposition temperature must be relatively high (200-210°C).
Polycaprolactone - PCL	Low melting, extremely flexible material, good bonding between layers.	The low melting temperature is an energy advantage, but the material transition from a soft to a solid state requires a long time. The soft-state material's high viscosity creates friction during deposition stressing the plotting motor. It is not stretchable during deposition (limiting a differential deposition for bending).
Acrylonitrile butadiene styrene - ABS	Relatively flexible but at the same time rigid material that can potentially ensure a good body structure.	It is not biodegradable and requires too much high deposition temperature (about 230°C), stressing too much the whole system.
Polyvinyl alcohol - PVA	It could be an environmental-friendly solution since it dissolves entirely with water.	Extremely stiff. The feeding motor is highly stressed. It frequently causes breakages and requires too high deposition temperatures (about 240°C)
Thermoplastic polyurethane - TPU	Highly elastic material that does not create any mechanical stress in feeding or deposition.	It is not biodegradable and requires high temperature (about 220°C). This high elasticity negatively affects the body's structural properties: very irregular, bad layers adhesion, and not stiff enough to sustain the tip weight.

Data file S1. The GitLab repository (https://gitlab.iit.it/EDelDottore/gb_filobot) and the Zenodo repository (10.5281/zenodo.10287323) contain the Julia code used to generate the 3D Dubin paths, the MATLAB code developed to test the different paths generated to analyze the workspace of the growing robot, and a Windows installer to obtain the FiloBot simulator application developed for ease-of-use to test the different climbing plant-inspired behaviors presented in the main manuscript.